Stony Brook University

Defect Studies and Optimization of CVD Grown Boron Phosphide Films on Different Substrates

A Thesis Presented

by

Xuejing Wang

to

The Graduate School

in Partial Fulfillment of the

Requirements

for the Degree of

Master of Science

in

Materials Science and Engineering

Stony Brook University

December 2015

Stony Brook University

The Graduate School

Xuejing Wang

We, the thesis committee for the above candidate for the

Master of Science degree, hereby recommend

acceptance of this thesis.

Michael Dudley – Thesis Advisor

Professor, Department of Materials Science and Engineering

Balaji Raghothamachar – Second Reader

Research Professor, Department of Materials Science and Engineering

T.A. Venkatesh – Third Reader

Associate Professor, Department of Materials Science and Engineering

This thesis is accepted by the Graduate School

Charles Taber

Dean of the Graduate School

Abstract of the Thesis

Defect Studies and Optimization of CVD Grown Boron Phosphide Films on Different Substrates

by

Xuejing Wang

Master of Science

in

Materials Science and Engineering

Stony Brook University

2015

Boron phosphide (BP), a light III-V indirect semiconductor compound with medium band gap of 2.0 eV, has emerged as a promising material with its applications in solid-state neutron technology and semiconductor devices in extreme conditions. Since bulk BP is unavailable, heteroepitaxial film growth is being attempted on various substrates including silicon, silicon carbide (4H, 6H, 3C polytypes), AlN and sapphire of different orientations to determine the best substrate for growing high quality thin films. By investigating the defects (e.g. twins and grain boundaries, threading dislocations, stacking faults, inclusions) present in the BP epilayer using synchrotron white beam X-ray topography (SWBXT), high resolution X-ray diffraction (HRXRD), high resolution transmission electron microscopy (HRTEM) as well as other characterization techniques, the aim of this study is to gain insight on defect nucleation mechanisms, and develop strategies from the control of growth parameters (temperature, flux rate, reaction time, P/B ration) and the nature of substrate (Si or SiC, polytype of SiC, off-cut angle and direction) to achieve higher single crystalline quality for fabrication of neutron detectors. Detailed studies are listed below.

1) Defect studies of CVD grown BP epilayer on c-plane SiC substrates.

BP heteroepitaxial layers were grown by chemical vapor deposition (CVD) technique on 3C-SiC, 4H-SiC, and 6H-SiC substrates, among which 3C-SiC was grown as the buffer layer on Si to improve its quality and stability. Growth parameters varied from substrate off-cut angle, growth temperature, P/B ratio and growth time. SWBXT study revealed the basic epitaxial relationships of the BP||SiC films. These were found to be $(100)_{BP}||(100)_{3C\text{-}SiC}$, $(111)_{BP}||(111)_{3C\text{-}SiC}$, $(111)_{BP}||(0001)_{4H\text{-}SiC}$ with 4° off-axis along $<1\bar{1}00>_{4H\text{-}SiC}$ or 8° off-axis along $<1\bar{1}00>_{4H\text{-}SiC}$, $(111)_{BP}||(0001)_{6H\text{-}SiC}$ with 3.5° off-axis along $<1\bar{1}00>_{6H\text{-}SiC}$. The diffraction spots confirmed the single crystalline nature and displayed the general quality of the films. BP diffraction spots,

compared to that of SiC substrates, were generally more blurred and overlapped with the some 4H-SiC, 6H-SiC and 3C-SiC diffraction spots. Comparison of the observed diffraction patterns with LauePt-simulated patterns of expected compounds revealed the presence of twinned and matrix BP epilayer domains on c-plane 4H-SiC and 6H-SiC substrates, related by a 180° rotation. Also, some unmatched diffraction spots recorded on the patterns indicate the likelihood of $B_{12}P_2$ inclusions. Grazing incidence topographs recorded from these layers were not able to effectively reveal detailed microstructure due to large strains. From the SEM observations, surface roughness and structure differed in each substrate and could be influenced by the growth conditions and substrate type. Among all the samples, $(100)_{BP}||(100)_{3C\text{-}SiC}$ film revealed the best surface smoothness, which corroborates the HRXRD measurements that $(100)_{BP}||(100)_{3C\text{-}SiC}$ showed lowest FWHM values as well as high epitaxial diffraction intensity. Extensive high-precision measurements of relative out-of-plane lattice mismatch have been conducted, and the high quality (100) BP heterofilms were found to be almost relaxed through the strain-induced defects. Reciprocal space mapping of selected high quality samples suggested that there was no rotational misorientation between the film and substrate. TEM studies on $(100)_{BP}||(100)_{3C\text{-}SiC}$ confirmed the existence of (0001) $B_{12}P_2$ and its twins, dislocations and stacking faults. Smooth atomic connection was observed at the interface region, without any intermediate layer or second phase. All the results indicate good crystalline quality of $(100)_{BP}||(100)_{3C\text{-}SiC}$ and can be potentially applied to devices.

2) Defect studies of CVD grown BP epilayer on c-plane AlN/Sapphire substrates.

The CVD grown AlN-buffered sapphire films were basically divided into two categories: on-axis $(111)_{BP}||(0001)_{AlN}$, and 1° off-axis $(111)_{BP}||(0001)_{AlN}$. Growth temperatures such as P/B ratio and growth time were varied between samples for comparison. SWBXT revealed the basic epitaxial relationship, which was $(111)_{BP}||(0001)_{AlN}$ with 1° off along $<11\bar{2}0>$. Again, diffraction patterns revealed the presence of twinned and matrix BP epilayer domains on c-plane AlN-buffered sapphire substrates, with a 180° rotation on [0001]. SEM images showed high surface smoothness, which corroborated the HRXRD rocking curve measurements, with relatively low FWHM values and the high peak intensities of the BP epilayer. Extensive high-precision measurements of relative in-plane lattice mismatch have been conducted, and the on-axis heterofilms were found to be almost relaxed through the strain-induced defects. Reciprocal space mapping of selected high quality samples suggested that there was no rotational misorientation in the films. General results demonstrate a better quality of the BP||AlN system compared with that of BP||SiC system.

Table of Contents

List of Figures

List of Tables

List of Abbreviations

B	Boron
P	Phosphorous
BP	Boron phosphide (monophosphide)
$B_{12}P_2$	Boron subphosphide
SiC	Silicon carbide
AlN	Aluminum nitride
CVD	Chemical vapor deposition
SWBXT	Synchrotron white beam X-ray topography
DP	Diffraction pattern
SEM	Scanning electron microscopy
HRXRD	High resolution X-ray diffraction
FWHM	Full width at half maximum
RSM	Reciprocal space mapping
TEM	Transmission electron microscopy
HRTEM	High resolution transmission electron microscopy
SAD	Selected area diffraction
STEM	Scanning transmission electron microscopy
FIB	Focused ion beam

List of Symbols

d	d-spacing
θ_B	Bragg angle
λ	Wavelength
m_{th}^*	Theoretical lattice mismatch
m_{real}^*	Real lattice mismatch
τ	Strain
w	Full width at half-maximum (FWHM)
w_s	Symmetrical FWHM
$\sqrt{\frac{\lvert\gamma_h\rvert}{\gamma_0}}$	Deviation parameter of FWHM

Acknowledgments

First I would like to give my deep and sincere gratitude to my advisor Prof. Michael Dudley, for providing me great opportunity working in the group and bringing me to the area of defect characterization of thin films. He provides guidance not only towards the research work, but also towards the life and the future which I feel really appreciated.

Second I would like to thank Prof. Balaji Raghothamachar for his patient guidance during research. His encouragements and suggestions make me surpass myself and fully developed during the research studies.

I would like to thank my lovely parents for their patience, support, guidance, and understanding during my master's study. Without them I cannot have this great experience in the USA.

I would like to thank Prof. T.A. Venkatesh for being the reviewer of my master's thesis.

I would like to thank Dr. Dong Su, Dr. Kim Kisslinger, and Dr. Dmytro Nykypanchuk for their great help on TEM and XRD experiments at Brookhaven National Lab.

I would like to thank Balabalaji Padavala, C.D. Frye, Neelam Khan, and J. H. Edgar for their great collaborations and providing all the samples for investigation.

I would like to thank my boyfriend Zheng Zhang for his encouragements and suggestions during my research work. He strengthened my confidence of doing research in Materials Science.

I would like to express my sincere thanks to all my colleagues, Dr. Yu Yang, Dr. Jianqiu Guo, Dr. Ouloide Goue, for all their helps during my research.

Financial support: the use of the National Synchrotron Light Source, Brookhaven National Laboratory, was supported by the U.S. Department of Energy, Office of Science, Office of Basic Energy Sciences, under Contract No. DE-AC02-98CH10886. This research used resources of the Center for Functional Nanomaterials, which is a U.S. DOE Office of Science Facility, at Brookhaven National Laboratory under Contract No. DE-SC0012704.

Chapter 1. Introduction

1.1 Motivation

The semiconducting properties of Si and Ge have generated considerable interest in the III-V compounds, but boron-based compounds such as boron arsenide and boron phosphide were not well-known semiconductors because of the relatively large energy gaps and their extreme difficulty of preparation. Boron and phosphide used to be the common doping materials for n-type or p-type semiconductor device, until 1950 when Nature [1] first published the structure of boron phosphide compound and its reaction process. In 1959, Forrest V. Williams [2] demonstrated the synthesis, physical and chemical properties of boron phosphide and arsenide in detail. During the same time, NASA [3] reported their collaborated results on boron arsenide and phosphide, especially their applications in high temperature and luminescent devices, such as Schottky barriers, metal-insulator-boron phosphide structures, and p-n junctions. With relatively large energy gaps, boron-based devices should be capable of operation at much higher temperatures than silicon devices. The most obvious advantage of boron compounds might be its application in solid-state neutron detection technology. With high neutron cross-section (3840 barns) and natural abundance of $^{10}B(n, \alpha)$, ^{10}B-based semiconductor detector is supposed to be the best substitution of the conventional ^{3}He gas-filled detector. Developing high quality BP thin films for neutron detector applications is the substantial and the most crucial step because defect density would influence electronic properties and device performance. This motivation drives us to apply different characterization techniques to study the structure of defects in order to optimize the crystalline quality during thin film deposition process.

1.2 Background of boron phosphide

Boron phosphide (commonly referred to cubic monophosphide, BP) is a light indirect III-V semiconductor compound with a medium band gap of 2.0 eV [4]. As mentioned before, boron phosphide possesses zinc blende structure, which comprises 50% boron atoms (B) and 50% phosphide atoms (P) (Fig. 1-1(a)). The lattice parameter of BP is 4.5383 Å. Previous studies have demonstrated the outstanding properties of BP [5]-[9]. For example, pure boron phosphide is predicted to be colorless, much like diamond. It is a refractory material with hardness higher than SiC. It has low atomic mass and strong interatomic bonding with low anharmonicity, iconicity, and high Debye temperature. It also possesses high thermal conductivity and stability and potentially applicable to thermoelectric devices. Charge carrier mobility and lifetime limit the performance and also the devices that can be fabricated. Kumashiro [9] reported a high charge carrier concentration of 1018 to 1021 cm^{-3} and high carrier mobility of 4.7×10^{18} cm^{-3}.

Another common polymorph is boron subphosphide ($B_{12}P_2$) that has an icosahedral structure (Fig. 1-1(b)). This icosahedral boride does not follow the general bonding rules, instead, the internal bonding is based on an electron-deficient three-center bonding scheme whereby two electrons are shared among three boron atoms. $B_{12}P_2$ has a wide band gap of 3.3 eV, and melting point of 2120 °C, which suggests it can be applied to high temperature devices. However, the low charge carrier mobility and thermal conductivity as well as high resistivity make $B_{12}P_2$ undesirable during BP synthesis [10][11]. Only the boron monophosphide (BP) has been researched thoroughly and demonstrated to have great potential for detector applications.

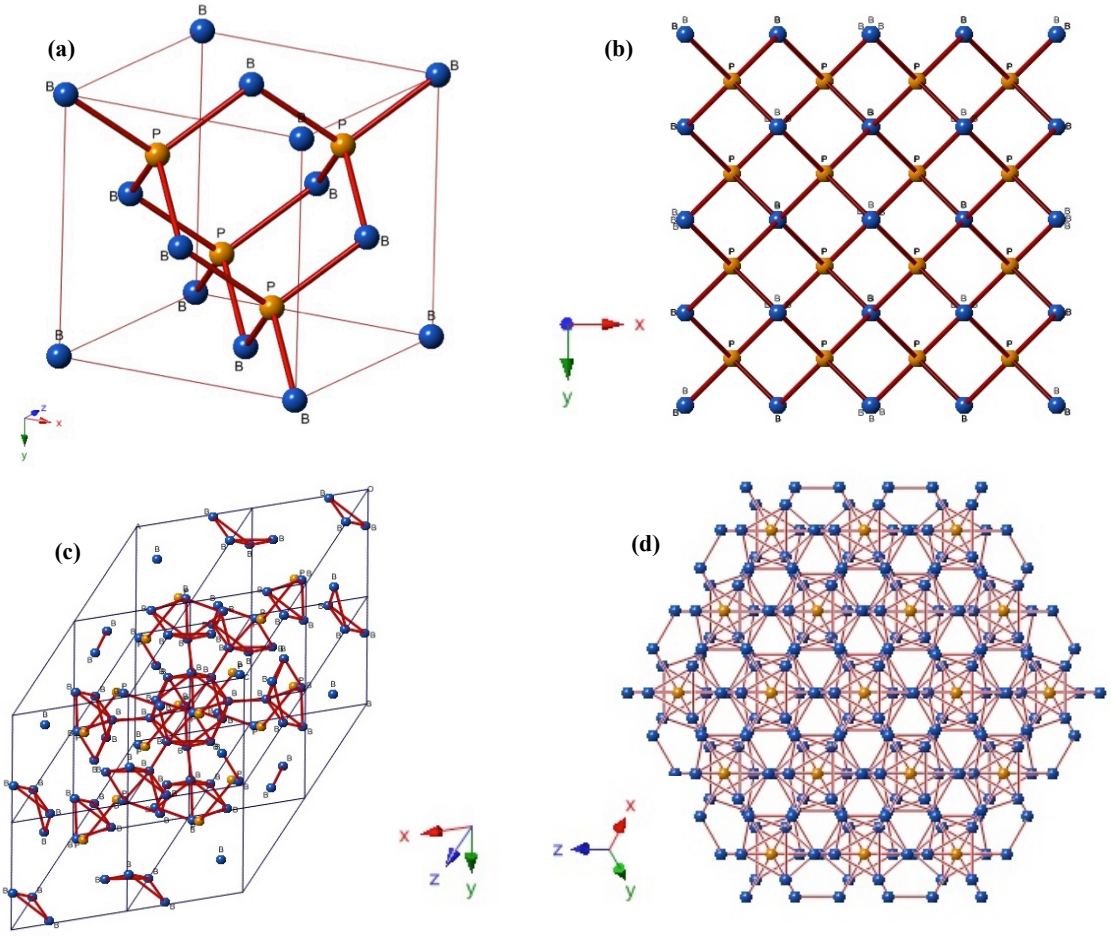

Fig. 1-1 Crystal structure of (a) BP: zinc blende structure, (b) (100) BP atomic projection, and (c) $B_{12}P_2$ rhombohedral structure; (d) (111) $B_{12}P_2$ atomic projection

Basic structure and properties of BP, $B_{12}P_2$ as well as other B-based compounds are concluded as below (Table. 1-1).

Table. 1-1 Properties of selected boron compounds

	BP	B_4C	BAs	$B_{12}As_2$	BN
Color	Reddish brown, transparent	Orange, yellow	Dark brownish	Amber, transparent	Black, golden
Structure	Cubic	Rhombohedral	Cubic	Rhombohedral	Cubic
Lattice Parameter a; c (Å)	4.5383	5.6; 12.12	4.777	6.156; 11.929	3.615
Melting point (°C)	>3000	2450		2027	
Band gap (eV)	2.0 (Indirect)	2.5	1.46	3.34	6.4 (Indirect)
Resistivity (Ω-cm)	P-type, 10~12.5 N-type, 0.15~2.5	0.1~10	P-type, 0.01	P-type, 10^4-10^5	P-type, 1~1000 N-type, 1~1000
Thermal Conductivity (W/cm-K)	4.0	0.29-0.67		1.2	4.7
Mobility (cm^2/V sec) Holes-Electrons	20~350 107~120	<1	100~400	80	0.2~-4

1.3 Substrate selection

The current absence of homoepitaxial growth of BP necessitates the heteroepitaxial thin film growth on various substrates. Epitaxial growth of BP on various substrates including Si, SiC polytypes, GaN, AlN and sapphire have been attempted and successfully reported. General information of all the substrate materials is included in Table. 1-2. These materials are selected as active substrates primarily because of their dimensional stability, which means relatively insensitive to environmental conditions. Dimensional stability is a critical requirement for sensors and actuators with high precision. Besides stability, parameters such as lattice mismatch and difference in thermal expansion coefficient (CTE) would always induce either compressive or tensile strain during the heteroepitaxy. These strains would generate defects from the interface but will act as relaxation effect. Usually better relaxation effect would improve the thin film quality. But the presence of defect would influence the performance for devices. For years people are trying to design the best material for minimizing defects.

Table. 1-2 Properties of BP and common substrate materials

	BP	GaN	AlN	Si	3C-SiC	4H-SiC	6H-SiC
Structure	Z. B	Wurtzite	Wurtzite	Diamond	Z. B	Wurtzite	Wurtzite
Band gap (eV)	2.0 (Indirect)	3.4 (Indirect)	6.2 (Direct)	1.1	2.39 (Indirect)	3.2	3.1
Lattice constant, a, c (Å)	4.538	3.189, 5.185	3.112, 4.982	5.431	4.3596	3.07, 10.05	3.07, 15.11
Density (g/cm^3)	2.94	6.1	3.26	2.33	3.17	3.211	3.21
Mohs Hardness	9.3			7			9.2-9.3
CTE (10^{-6} K^{-1})	~3.6	5.59	5.3	2.6	3.9	4.0	4.0
Melting point (°C)	>3000	>1700	3000	1415	3103	3103	3103
Thermal conductivity (W/cm×K)	4.0	1.5	2	1.5	3.5	3.7	4.9

Silicon is the most popular choice of substrate material and has been attempted for BP epitaxial growth since 1971 (Chu et al) [12]. Primary reasons for the silicon application include its mechanical and thermal stability, low thermal expansion coefficient, and flexibility of electronics

integration. But since the lattice mismatch between BP and Si is large (≈ **17**%), strain-induced defects during the crystal growth limit the BP quality and the device properties. But Si is applied in many cases as substrate material to grow the thin film buffer due to its stability and relative maturity of growth.

Investigations of silicon carbide single crystals for heteroepitaxial growth of BP start from recent years. [13] With the improvement of SiC growth, the 4H-SiC and 6H-SiC obtained much higher single crystalline quality with controlled defect intensity. Similar with silicon, the principles for application of silicon carbide (SiC) and include its dimensional and chemical stability at high temperatures. SiC exists in about 250 crystalline forms, and the polymorphism of SiC is characterized by a large family of similar crystalline structures called polytypes. The common polytypes under investigations are 4H-SiC, 6H-SiC, 15R-SiC and 3C-SiC, which possess varied structures and stacking sequences (Figure. 1-2). Both 4H-SiC and 6H-SiC possess the wurtzite structure. C-plane substrates with atomic-scale steps have been applied as comparison to on-axis ones and have proved higher quality for growing boron arsenide ($B_{12}As_2$) thin films. [14][15] Development of 3C-SiC is relatively limited because of the difficulty during synthesis, so currently the 3C-SiC is usually grown as the buffer layer on Si substrates. In our studies, we have done a comprehensive analysis on BP grown on (100) 3C-SiC and proved it to be a good candidate substrate material.

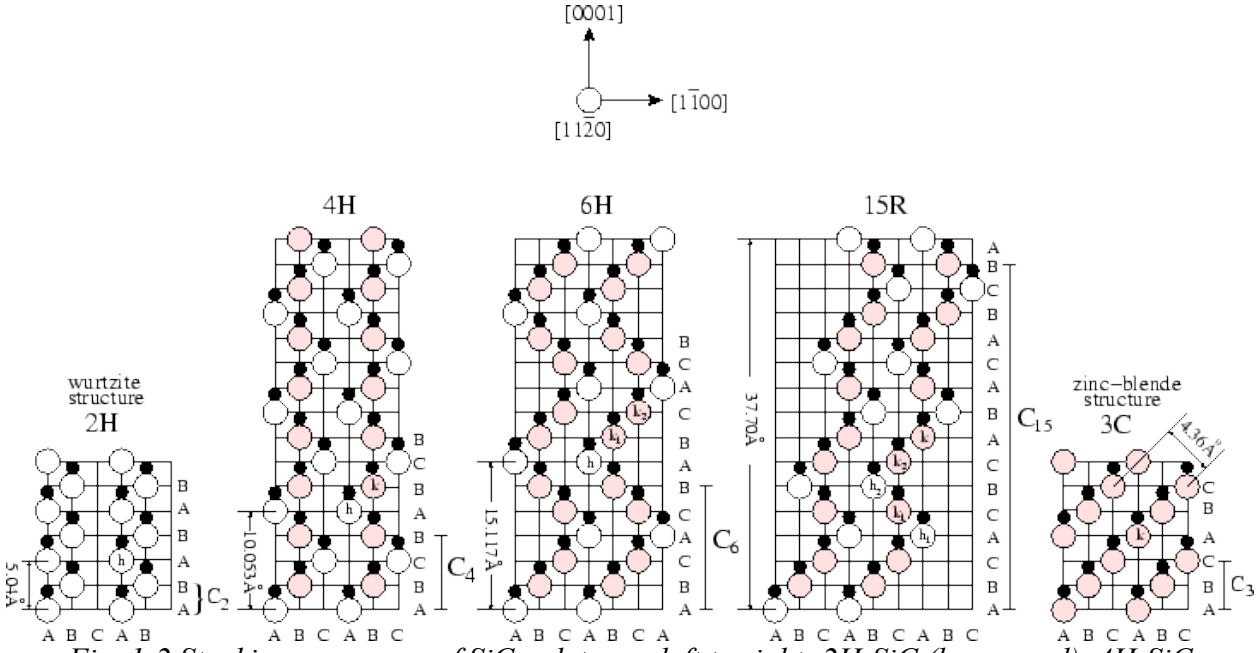

Fig. 1-2 Stacking sequences of SiC polytypes, left to right: 2H-SiC (hexagonal), 4H-SiC (hexagonal), 6H-SiC(hexagonal), 15R-SiC(hexagonal), and 3C-SiC (zinc blende)

1.4 Epitaxy and growth technique

The basic principle of epitaxy is oriented overgrowth of a single crystalline material on top of a single crystal substrate. The grown material can either be the same (homoepitaxial) or different (heteroepitaxial) from the substrate. Compared with other deposition methods, the epitaxial growth has wide applications in fabricating semiconductor junctions. It has several advantages such as lower processing temperature, more accurate control of dopant concentration and

distribution, and can realize epitaxial junctions with lower impurities. Epitaxial growth is particularly suitable for III-V compound semiconductor junctions, and thus desirable for developing BP semiconductor-based neutron detectors.

Both physical vapor deposition (PVD) or chemical vapor deposition (CVD) are able to synthesize epitaxial layers. The CVD technique (Fig. 1-3) has been applied to more extensive uses include conductor layers, semiconductors and insulators. [16][17] It can be carried out in either a closed system or an open flow system, but open flow system can provide growth flexibility with well-controlled dopant concentration and distribution. [3] The flow system involves a substrate held at suitable temperature in a reaction chamber provided with a gas inlet and exhaust. During the reaction, gaseous mixtures containing the constituents of the desired material are introduced into the reaction chamber, the product from the chemical reaction would be deposited onto the substrate surface, and this is the general theory of how CVD works. The growth process is generally described as the following steps:

1) Mass transfer of the reactants to the substrate surface; (rate determining step)

2) Adsorption of the reactants onto the substrate surface;

3) The reaction or series of reactions on the surface;

4) Desorption of the by-product molecules;

5) Mass transfer of the by-product molecules from the surface.

Reactants are required to be amenable to purification, and also chemically inert towards the chamber wall. Furthermore, the chemical reactions should be controlled carefully that vapor deposition takes place predominantly on the substrate surface. The morphology and quality of the epitaxial layers depend on the deposition conditions, quality and nature of the substrate. For example, at very low temperatures, kinetics is not favorable for epitaxial growth which usually leads to amorphous growth. As the deposition temperature increased, epitaxial growth would become favorable due to the kinetic factors. But when temperature is too high, it will adversely affect crystallinity and the composition of the deposit.

Owing to the high melting point and thermal instability, the most common and technique for BP heteroepitaxial growth is the conventional CVD, although other techniques such as solution growth [16] and metalorganic vapor phase epitaxy (MOVPE) [13] also been attempted successfully. CVD is the most convenient way of producing poly or single crystalline boron phosphide. Initially four possible reactions have been considered to be potentially useful: 1) the thermal decomposition of a diborane and phosphine mixture, 2) The reaction of boron tribromide and phosphine, 3) The reaction of diborane with phosphorus trichloride, 4) Thermal reduction of a boron tribromide-phosphorus trichloride mixuture. Chemical reactions are written below respectively:

1) $B_2H_6(g) + 2PH_3(g) \rightarrow 2BP(s) + 6H_2(g)$;
2) $BBr_3(g) + PH_3(g) \rightarrow BP(s) + 3HBr(g)$;
3) $B_2H_6\ (g) + PCl_3\ (g) \rightarrow 2BP(s) + 6HCl(g)$;
4) $Br_3(g) + PCl_3(g) + 3H_2(g) \rightarrow BP(s) + 3HCl(g) + 3HBr(g)$;

Deposition experiments utilizing these reactions are carried in the apparatus shown in Fig. 1-3.

Compare four reactions together, the reactions 1) and 4) are suitable reactions of producing high quality single crystalline BP films. Growth reactions of 1) and 4) are 15 μm/hr and 60 μm/hr, which indicate long reaction time and cost of the growth process.

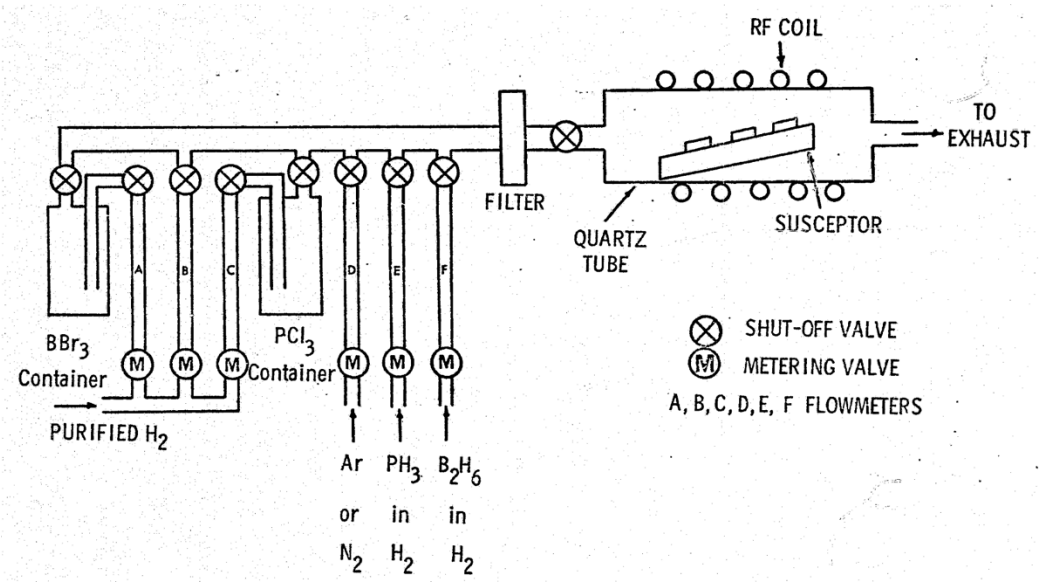

Fig. 1-3 Schematic diagram of chemical vapor deposition technique (CVD)

1.5 Solid state neutron detector

Detection of neutrons is fundamental to the advance of subfields within nuclear medicine, high-energy physics, non-proliferation of special nuclear materials, astrophysics, structural biology and chemistry, magnetism and nuclear energy. [18] Since neutrons do not react with matters through Coulomb forces, neutron detection can only be realized through nuclear reaction products generated from neutron absorption events. The reaction products include alpha particles, gamma rays, nucleons, heavy and light ions. [19] These products would travel through the detection media and generate secondary reaction products by ionizing and exciting atoms they encounter along the path. Then the primary and secondary reaction products will contribute to electrical signals.

The primary consideration for thermal neutron detector design is the interaction between detector materials with slow neutrons, which introduces an important factor: thermal neutron absorption coefficient (also called thermal neutron cross-section). The term describes the likelihood of interaction between an incident neutron and a target nucleus, the standard unit for measuring the cross section is barn, which is equal to 10^{-28} m^2 or 10^{-24} cm^2. Due to the large thermal neutron cross-section of ^3He (5337 barns) and insensitivity to background gamma radiation, ^3He was applied conventionally as the converter gas for high efficiency neutron detection (> 70%). [20] A ^3He gas-filled detector is shown in Fig. 1-4.

Basic principle of gas-filled thermal neutron detector is described as follows. Gases are used in radiation detectors since their ionized particles can travel more freely than those of liquid or solid. The central electrode (or anode) collects negative charges. A voltage is applied through the anode to the chamber walls. The resistor in the circuit is shunted by a capacitor in parallel, so that the anode is at a positive voltage with respect to the detector wall. As a charged particle passes through the gas-filled chamber, it ionizes some of the gas along its path of travel. The positive anode attracts the electrons (negative particles). The detector wall, or cathode, attracts the positive charges. The collection of these charges reduces the voltage across the capacitor, causing a pulse across the resistor that is recorded by an electronic circuit. The voltage applied to the anode and cathode determines the electric field and its strength. When the applied voltage is high enough, the ion pairs initially formed accelerate to a high enough velocity to cause secondary ionizations. The resultant ions cause further ionizations. This multiplication of electrons is called gas amplification.

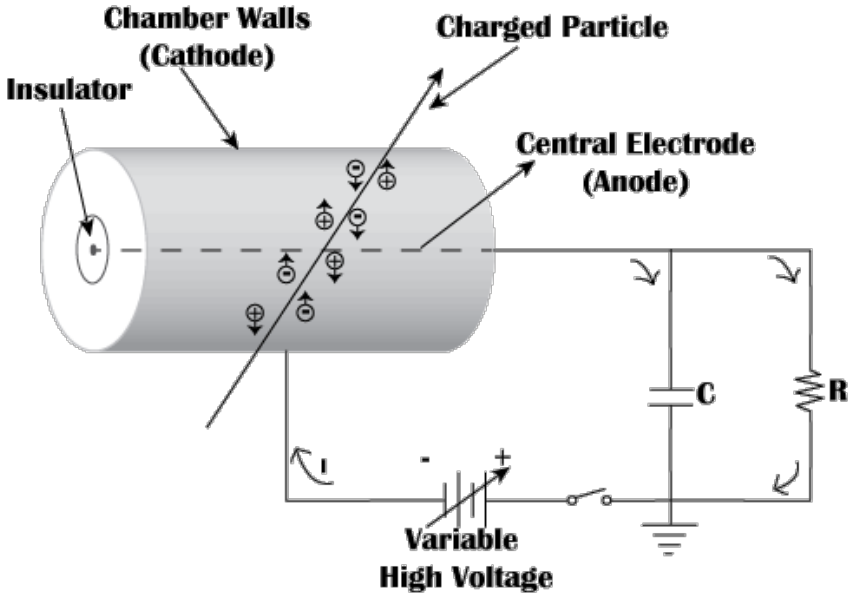

Fig. 1-4 Conventional ^{3}He gas-filled thermal neutron detector

However, the recent major increase in demand of neutron detection as well as the dwindling U.S. stockpile of ^{3}He arises challenges in neutron detector technologies. Substituent materials and new designs are the alternative solutions to the problem, which comes to the development of solid state neutron detectors. The semiconductor-based neutron detectors also called solid-state or thin film coated neutron detectors. But conventional semiconductor materials have very low interaction with free neutrons. For example, the thermal neutron cross-section of Si is only 2.24 barns, which means a thermal neutron would have to travel an average distance of 8.6 cm (mean free path) before scattering or capture would occur. This makes electronic materials such Si ineffective in detector application. However, compared with gas-filled neutron detectors, the semiconductor based neutron detectors are still desirable since they are more compact, inexpensive, can be operate at lower temperatures, and more robust against vibration induced noise.

Apart from ^{3}He, substituent isotopes have been developed, as indicated in Table. 1-3. From the table, ^{10}B and ^{6}Li are both potentially applicable since they have higher abundance and thermal neutron cross-sections.

Table. 1-3 Isotopes and the neutron detection properties

Isotope (% Abundance)	Charged Particle Produced	Q Value (MeV)	Thermal Neutron Cross-section	State of Material
^{10}B (19.9)	^{7}Li, α	2.78	3840	Solid
^{6}Li (7.59)	^{3}H, α	4.78	973	Solid
^{3}He (0.000137)	^{3}H, p	0.765	5337	Gas

The best way to overcome the poor interaction is to integrate a layer of neutron reactive material into the design of semiconductor architecture. This design is commonly refer to conversion layer devices, which use Si or GaAs p-n diode or Shottky diodes to separate electron-hole pairs generated from interactions with primary nuclear reaction products. The planar conversion layer p-n junction thermal neutron detector and its mechanism are shown in Fig. 1-5.

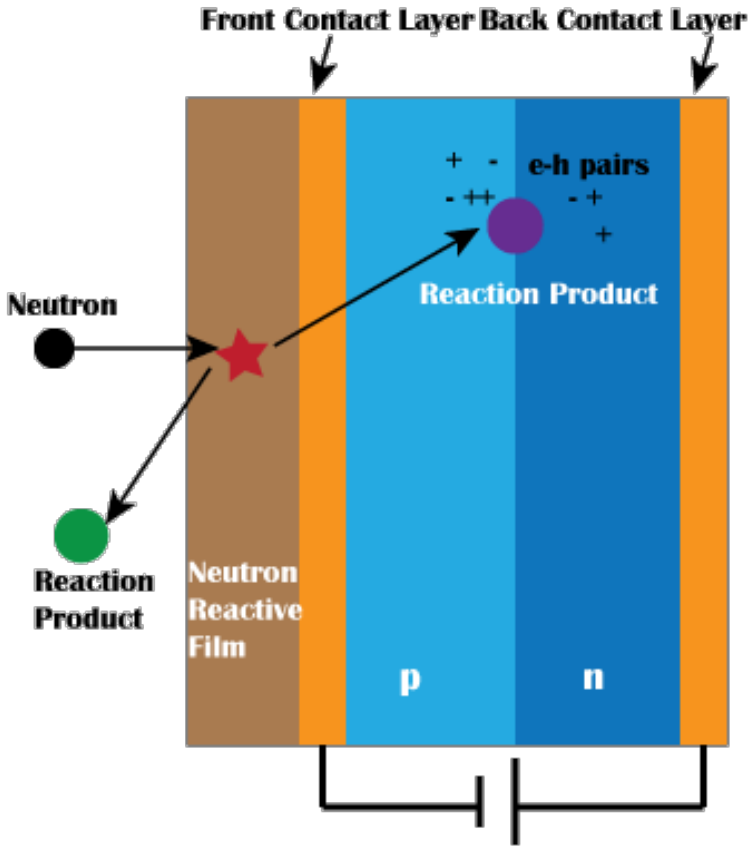

Fig. 1-5 Planar conversion layer p-n junction thermal neutron detector

Basic components include a semiconductor p-n diode, very thin front and back contact layers, and the neutron reactive layer (film). Its working function relies on second order effect. Reactions of ^{10}B with neutrons results in following products: [21]

94%: $^{10}B + n \rightarrow {}^{7}Li$ (0.840 MeV) + ^{4}He (1.470 MeV) + γ (0.48 MeV), Q = 2.310 MeV (1st excited state);

6%: $^{10}B + n \rightarrow {}^{7}Li$ (1.015 MeV) + ^{4}He (1.777 MeV), Q = 2.792 MeV (to ground state).

These two reaction products are released in opposite directions when thermal neutrons (0.0259 eV) are absorbed by ^{10}B. After the absorption, 94% of the reactions leave the ^{7}Li ion in its first excited state and de-excites to the ground state rapidly. The remaining 6% of the reactions result in the ^{7}Li ion going to the ground state.

The critical design for planar conversion layer based devices lies in the thickness of the conversion layer material since the ultimate destination is to maximize the thermal neutron detection efficiency. The conversion layer is expected to be thick for increasing the absorption magnitude, like for ^{10}B, ~90% of incident neutron flux will be absorbed in a ~50 μm thick layer. However, there is trade off effect. As the conversion layer thickness increases, the traveling distance for neutron reaction products would increase, with some absorbed before transfer into the p-n diode. It is also possible that if the layer is too thick, by the time reaction products reach the semiconductor they may not have enough energy for adequate electron-hole pair generation. In addition, the planar geometry of the device also restricts the primary reaction products that are able to contribute to e-h pair to 50%. As described before, the nuclear reactions are emitted at 180 degrees relative to one another, which means that only part of the products would be transduced into e-h pairs. [22] From materials science perspective, crystalline quality of both conversion layer and the p-n semiconductor is important. Controlling the defect density inside the films crucial to the device performance.

To resolve these problems, innovative three-dimensional semiconductor detector designs using photolithography and deep reactive ion etching (DRIE) have renewed interest in semiconductor-based technologies for high efficiency thermal neutron detection. For example, as is shown in Fig. 1-6, the pillar semiconductor based neutron detector reached detector efficiency to ~20% (expected to be >75%). This design can achieve maximum neutron absorption and while simultaneously providing the reaction products with a reasonable pathway to escape into the semiconductor. In addition, the p-i-n diode is applied to replace the p-n diode in order to enhance the charge collection efficiency and response time.

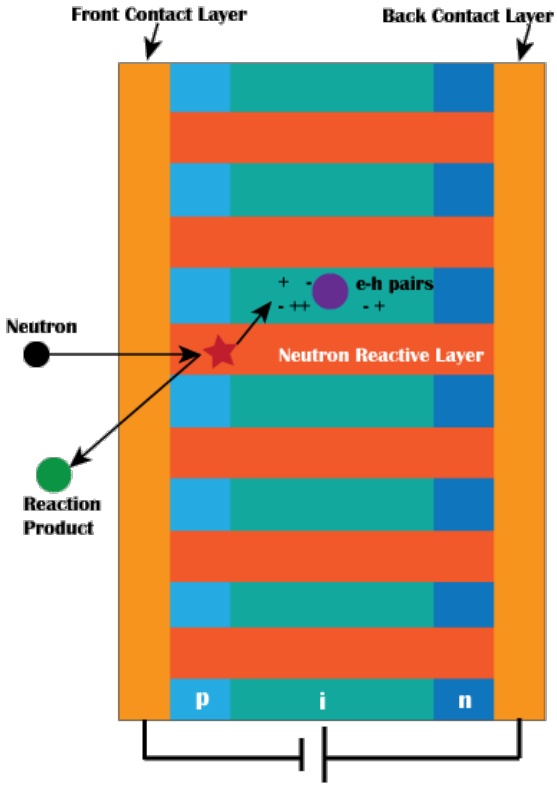

Fig. 1-6 Pillar semiconductor based neutron detector

1.6 Characterization techniques

1.6.1 Synchrotron white beam X-ray topography (SWBXT)

The X-ray topography (XRT) is a nondestructive technique for characterizing μm to cm sized defect microstructure of crystals by means of X-ray diffraction. [23] It is a powerful tool for the evaluation of crystals for technical applications and thin film growth and processing. Mechanism of this technique comes from the imperfection or deviation in structural uniformity inside the material. When X-ray beam passes through the crystal, localized variations in diffraction intensity realized different types of defects that cannot be observed visually. Previous studies on 4H-SiC and 6H-SiC wafers using X-ray topography have effectively observed defects including threading screw and edge dislocations (TSDs and TEDs), micropipes, basal plane dislocations (BPDs), stacking faults (SFs), etc. [24]-[29]

Main X-ray topography techniques include *Berg-Barrett* reflection (1931) [30], *Lang* (1958) [31] double-crystal technique [32], and its scanning oscillator technique [33]. In 1931, *Berg* carried out X-ray diffraction imaging on crystal surfaces using characteristic radiation falling at a very low angle to the crystal surface and obtained point-to-point variation of the reflected intensity, resulting in a striated image on a photographic place placed near the crystal. The striated images produced from plastic deformation inside crystals. Later *Barrett* recorded defect structure images from single crystals of silicon ferrite, he improved *Berg's* reflection technique by minimizing the distance between the crystal and the photographic emulsion plate and by using fine-grain high-resolution X-ray film. This technique is known as *Berg-Barrett* reflection topography (Fig. 1-

7(a)(b)) and is used to study large-size crystals. The transmission technique to image defects in crystals developed by *Lang* was a milestone in the field of X-ray topography. He examined crystal sections using a narrow collimated characteristic radiation beam, which refers to section topography. Linear and planar defects could be mapped with this technique by translating the specimen to known positions and taking a series of section topographs. By incorporating a linear traverse mechanism to translate the crystal plate and film cassette synchronously, *Lang* was able to image individual dislocations in an entire silicon crystal sample using projection topography (Fig. 1-7(c)). In the *Lang* technique, an incident beam of narrow width and low horizontal divergence is obtained using a slit. The secondary slit placed on the other side of the sample blocks the direct beam while allowing the diffracted beam to pass through. It is possible to obtain an image on the film using K_{α_1} only. This technique can permit up to 1 μm resolution under optimized conditions.

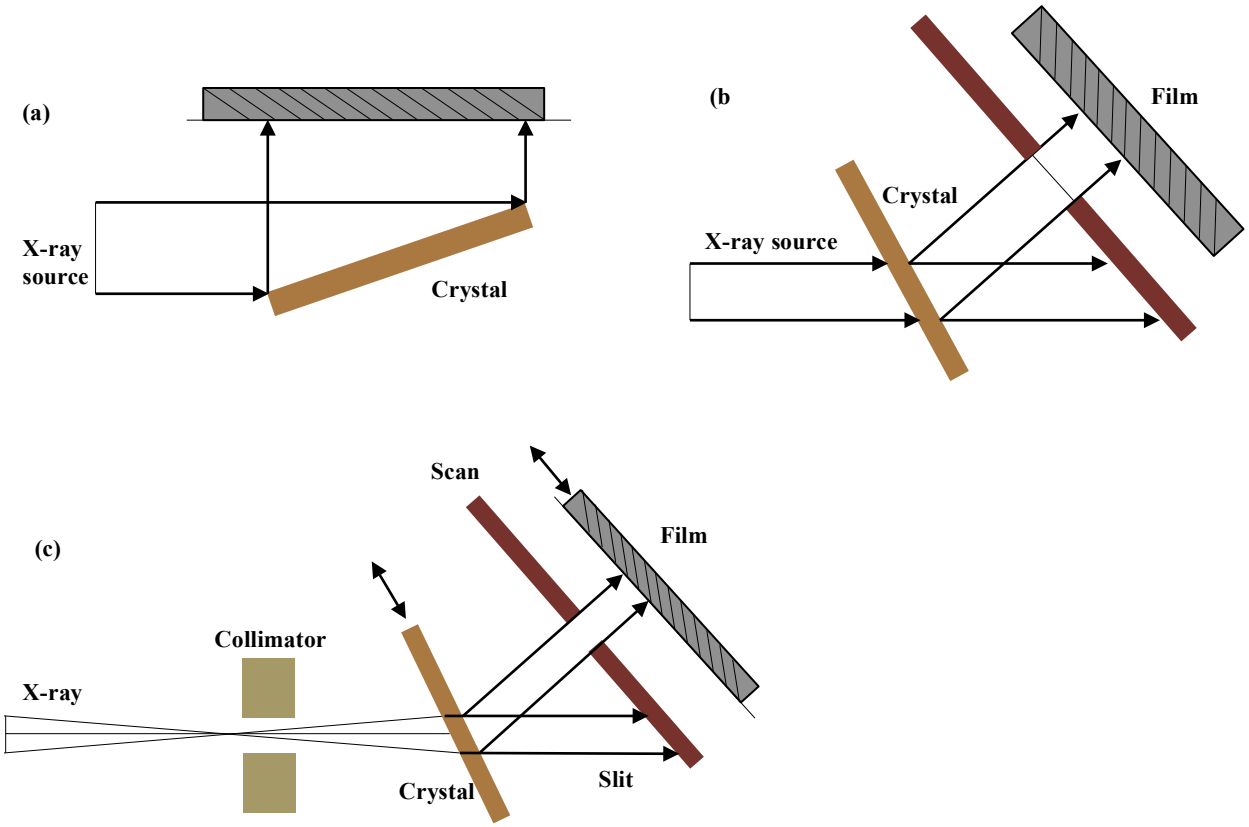

Fig. 1-7 Schematic diagrams of (a) reflection and (b) transmission Berg-Barrett techniques of topography, (c) Lang projection technique. The topography image due to K_{α_1} along is recorded on the film. The secondary slit blocks the direct beam while allowing the diffracted beam to pass through. The crystal and film are translated synchronously and the whole image of the crystal is recorded

The advent of synchrotron radiation enabled the development of new realm of topography known as synchrotron topography. It has numerous advantages over conventional radiation techniques such as high brightness, tenability and natural collimation. One of the most important synchrotron topographic techniques developed is white beam topography. Synchrotron white beam X-ray topography is similar to the Laue transmission technique, but has advantages such as natural collimation and high intensity of the synchrotron beam. The natural collimation allows very long beamlines as well as large beam area delivered at the sample, which in turn leads to excellent geometrical resolution capabilities. At Stony Brook Synchrotron Topography, Beamline X-19C at the National synchrotron Light Source (NSLS), the original beam passes through a 254 μm thick beryllium window as well as an 25.4 μm thick aluminum foil vacuum shield, result in an air path of 4 m. The spectral distribution has the maximum at 0.9 Å and is thus called synchrotron white beam X-ray. Effective source size is ($0.15\ mm \times 0.35\ mm$) and the long source-to-specimen distance is 25 m, which give rise to the spatial resolution of about 1.4 μm at a specimen-to-film distance of 10 cm. Synchrotron monochromatic beam can be obtained by applying the monochromator, which is usually a channel-cut, highly perfect Si single crystal. [34]

Basic imaging geometries applied in XRT are transmission geometry (Laue) and reflection geometry (Bragg), which includes back reflection and grazing-incidence diffraction geometry (Fig. 1-8). The reflection topography geometry is more suitable for thick crystals or when absorption conditions or defect densities are too high that transmission geometry is not effective. Owing to the surface sensitivity, the reflection geometry can also be applied to characterizing surface defects or structures of heteroepitaxial thin films. In transmission topography, all the defects within the crystal volume are recorded, provided that sufficient intensity is transmitted through the crystal. This geometry is suitable for characterizing bulk defects, and the synchrotron source will help to penetrate thick crystals with enough energy. [35]

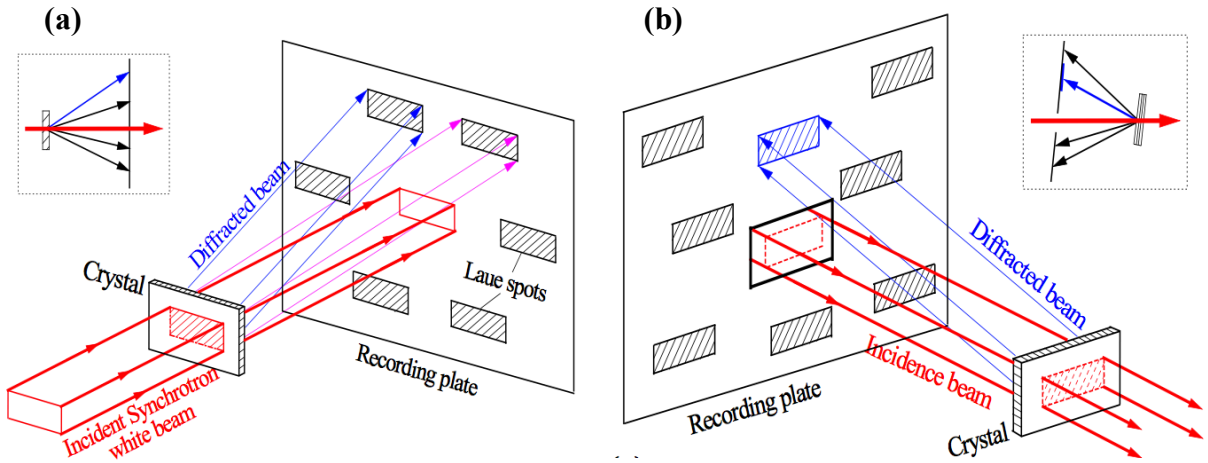

Fig. 1-8 Common X-ray topography geometries (a) transmission geometry (b) reflection geometry (back-reflection)

In this study, simulation of diffraction patterns uses the software LauePt [32], which is simple and effective for simulating diffraction patterns images recorded from X-ray topography. By loading the crystal structure from the database, DPs within certain orientation can be identified and

indexed. The settings of x, y, z axis as well as imaging distance can be adjusted in accordance with experiment conditions. Fig. 1-9 are examples of DPs from (0001) 4H-SiC with both transmission and back reflection modes.

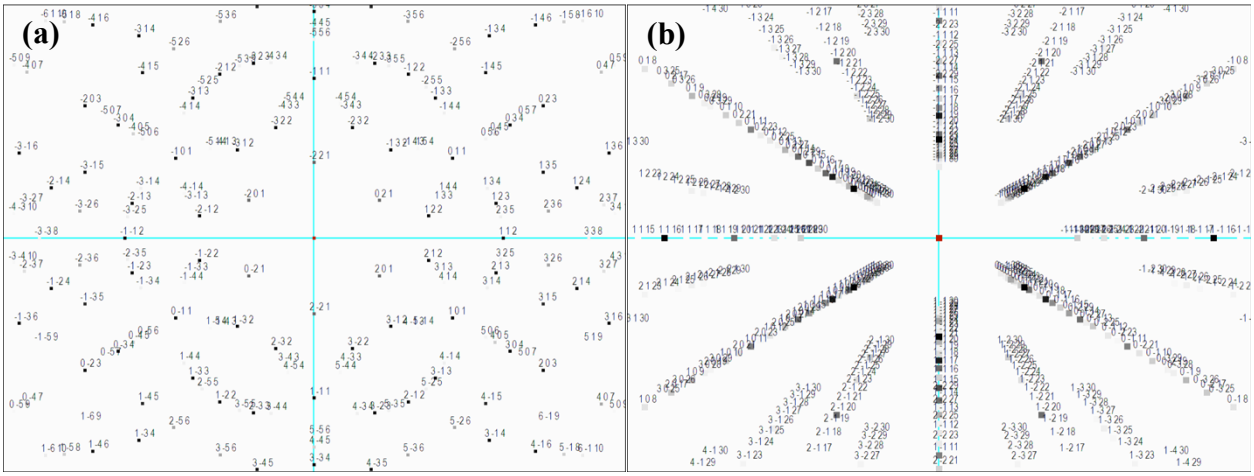

*Fig. 1-9 (a) Transmission X-ray simulated diffraction patterns (b) back reflection X-ray simulated diffraction patterns from (0001) 4H-SiC, side plane: (**$11\bar{2}0$**)*

1.6.2 Scanning electron microscopy (SEM)

SEM is a type of electron microscopy that produces images by scanning the sample with a focused beam of electrons. The electrons interact with atoms and produce various signals containing information about the sample's surface topography and composition. SEM can achieve resolution better than 1 nm. In our study this technique is mainly used for a general analysis of surface structure and morphology of the BP epitaxial layers.

1.6.3 High resolution X-ray diffraction (HRXRD)

HRXRD is generally used to investigate deviations from an ideal crystal which can be induced by defects, mosaicity or strain. Diffraction for a given plane and wavelength would take place by angular range characterized by the rocking curve width (FWHM), which varies tremendously and governs the strain sensitivity of the technique. Narrower FWHM value indicates higher quality of the sample. High resolution double axis rocking curve measurements use the Bede D1 X-ray diffractometor. Electrons are created by a filament and accelerated to the Cu target, from which X-rays are generated by a standard 2 kW sealed tube. Si (220) dual channel collimator and monochrometor are used for more precise scans.

The Ultima III Diffractometer at Center for Functional Nanomaterials at BNL is being applied to record triple axis rocking curves, from which the reciprocal space map (RSM) can be processed. From RSM, the lattice mismatch and the misorientation will be obtained.

1.6.4 Transmission electron microscopy (TEM)

TEM is the central tool for complete characterization of nanoscale (from <1 nm to ~100 nm) materials and devices. A TEM can generally appear in different forms such as high resolution TEM (HRTEM), scanning-TEM (STEM) from which individual columns of atoms in crystals can be resolved. Principle experiments in this study include the selected area diffraction (SAD), HRTEM and STEM as needed. SAD patterns inside the thin film would explain the presence of defects such as inclusions or twins, and also the general information of crystal parameters. High magnification images are crucial for obtaining the interfacial atomic stacking, which helps to understand the BP film growth mechanism as well as some defect growth mechanism. Crystal models with respect to different materials are built using the software CrystalMaker. It helps to realize atomic projections and flexible of changing orientations.

TEM requires ultra thin specimens, so that it can transmit sufficient electron intensity onto the CCD screen to interpret the images. This requires advanced techniques such as focused ion beam (FIB) or the conventional polishing and ion milling. The FIB instrument is becoming more readily available as prices moderate and their values is realized. General procedure of the in-situ lift-out is described in Fig. 1-10. First step is to find the marked area. A Pt bar is then deposited to protect this area from the Ga beam. Next, two staircases are cut out using the ion beam on either side to leave the thin wall, by doing a “U” cut, the wall will only be supported at the top. Then the specimen will be cut and stick on the Pt GIS needle. After attach the needle to the grid, the final step is to do the ion-polish until the thickness is ready for TEM specimens.

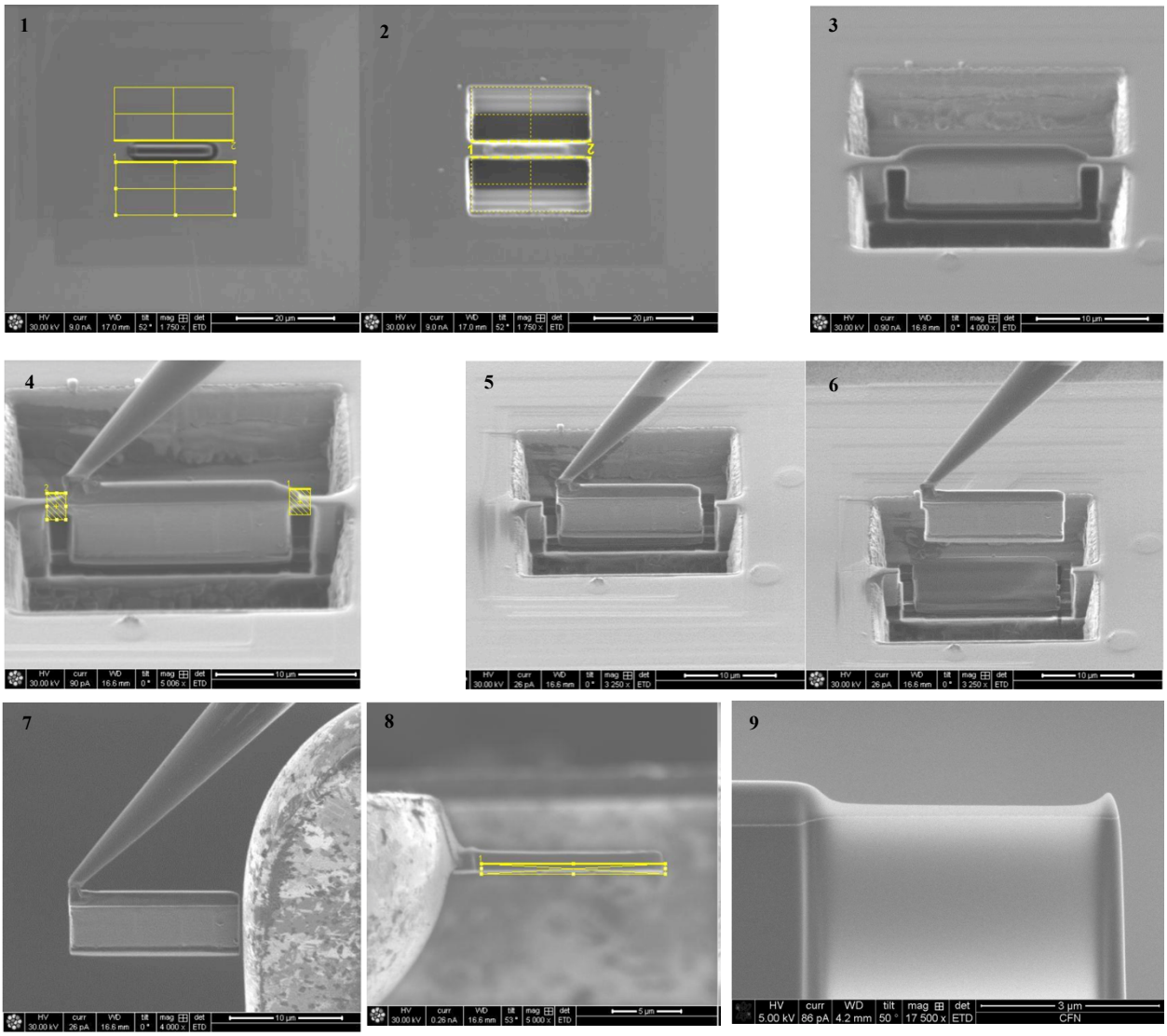

Fig. 1-10 In-situ lift-out procedure: 1~2：bulk milling using regular cross-section patterns, 3: make "U" cut by ion beam, 4: sample tabs being cut to free sample from substrate, 5~6: Lift-out of sample separating it from the substrate, 7: sample making very light contact with Omniprobe grid, 8: ion beam milling front and back of the sample, 9: TEM sample ready

For the mechanical polishing method, we use the instruments such as grinder-polisher and ion polishing systems. T-tool wedge polishing is being applied and its basic procedure is drawn in Fig. 1-11. As is shown in the figure, two pieces (~1.5 mm × 1 mm) are cut from the sample using low speed saw. Then these two pieces are stick together using the mixture of resin and hardener. Now the specimen is a sandwich structure with epilayers put together. Next step is to polish the specimen to the required thickness using the grinder polisher step by step. Using the diamond lapping films as well as suspension liquid, the polishing process should be careful and precise. Then the specimen is further thinned via dimpling technique and ion mill. Finally, a small hole is cut and would be ready for TEM experiments.

Compare two preparation methods, FIB is time-efficient and can greatly reduce the mechanical induced defects. However, for thick epitaxial layers, this technique is not advantageous because

general FIB uses the wedge cut, so that the bottom (substrate area) would be thicker compared with the top, which means if we want to take high quality HRTEM image at the interface, the specimen would be too thick. Mechanical polishing will resolve the problem since the thickness of the specimen would be controlled for interfacial analysis. But usually the hand-made TEM samples would induce some defects which may come from every single step, so that it take time and caution when using this preparation technique.

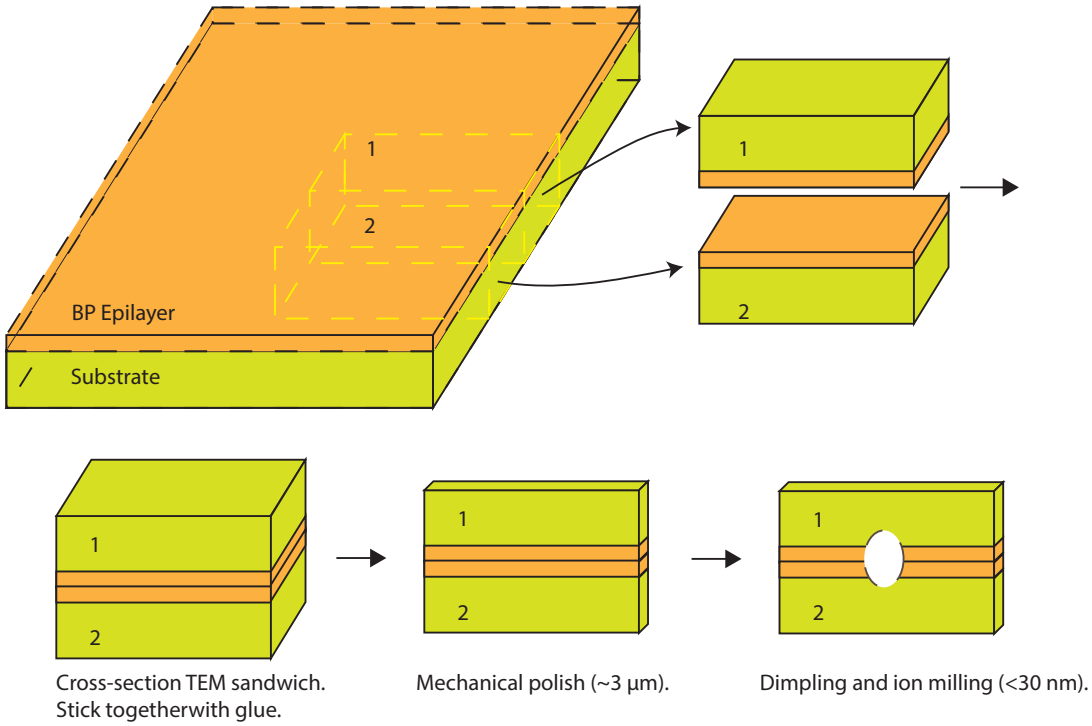

Fig. 1-11 Mechanical polishing method of TEM sample preparation

1.7 Calculations

1.7.1 Lattice mismatch

The basic principle of measuring lattice mismatch is to calculate both theoretical mismatch in ideal crystals and mismatch from the real crystals using the HRXRD data, and then compare the two values to get an idea of the strain relaxation inside the film. The general procedure includes a calculation of d-spacing values of both epilayer and substrate with respect to certain direction. In this study, all of the rocking curve measurements are based on symmetrical reflection, which means the mismatch will be calculated c direction and the strains are measured vertically. The drawback of this method is that the asymmetrical mismatch is not included. Scanning on asymmetrical reflection or/and doing triple axis rocking curve measurements are common solutions.

Combined with the Bragg's equation, d-spacing values can be calculated

$$2dsin\theta_B = n\lambda$$

Where n is a positive integer, λ is the wavelength of the incident wave and θ_B is the Bragg angle. Then the lattice mismatch (m^*_{th}) can be calculated from

$$m^*_{th} = \frac{d_{substrate} - d_{BP}}{d_{BP}} \times 100\%$$

For real mismatch values, it follows the same equations. But the difference is that we set either the substrate or epilayer as the reference (theoretical value). In this study, since we concentrate more on BP quality, so that BP epilayer will be set as the reference. The Bragg angle can be measured based on the angular distance between two peaks from ω-2θ rocking curves. Then the real d-spacing (d') is

$$d'_{sub} = \frac{n\lambda}{2sin\theta_B}$$

The real lattice mismatch will be

$$m^*_{real} = \frac{d'_{sub} - d_{BP}}{d_{BP}} \times 100\%$$

Compare real mismatch with theoretical one, the strain at the interface will be measured by

$$\tau = \frac{m^*_{real} - m^*_{th}}{m^*_{th}} \times 100\%$$

Results can be either positive or negative, indicates either the compressive strain or tensile strain.

1.7.2 Deviation in rocking curve half-width (FWHM)

In XRD measurements, the rocking curve half-width w (FWHM) is given by

$$w = \frac{2C\sqrt{\chi_h \chi_{\bar{h}}}}{sin2\theta_B} \sqrt{\frac{|\gamma_h|}{\gamma_0}}$$

As described before, the rocking curves are measured along c direction, which means the FWHM as well as the lattice mismatch are calculated from symmetrical reflection.

If w_s is the rocking curve for the symmetric reflection,

$$w = w_s \sqrt{\frac{|\gamma_h|}{\gamma_0}}$$

Where $\sqrt{\frac{|\gamma_h|}{\gamma_0}}$ is the deviation parameter varies from -1 to +1 in the range of total reflection.

For Bragg case (Fig. 1-12),

$$\gamma_0 = sin(\theta_B - \phi)$$

$$|\gamma_h| = sin(\theta_B + \phi)$$

So the deviation term $\sqrt{\frac{|\gamma_h|}{\gamma_0}}$ will be calculated. From this value we are able to measure the by how much the asymmetrical FWHM would be contributed to the total result.

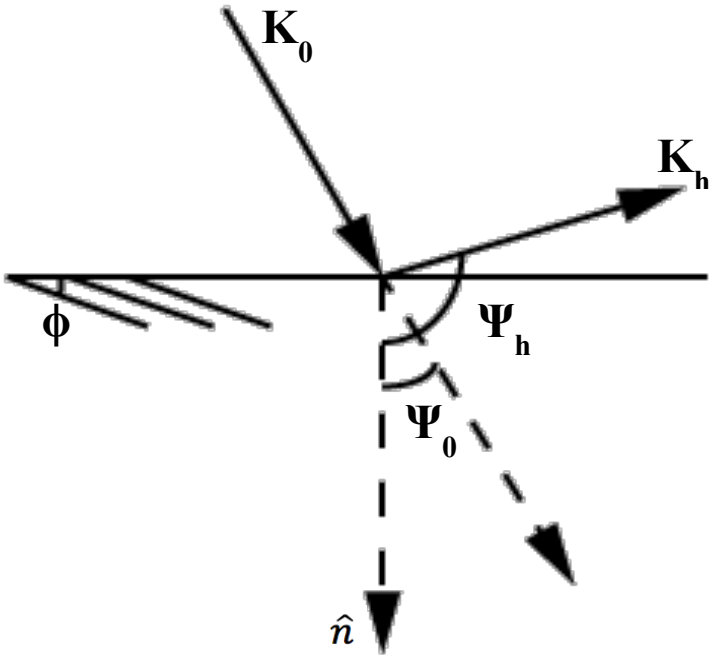

Fig. 1-12 Bragg diffraction diagram

Chapter 2. Defect Studies of CVD Grown BP Epilayer on 4H-SiC substrates

2.1 Outline

A detailed analysis of the crystalline quality and structure in BP epitaxial growth on 4H-SiC substrates is presented. A combination of SWBXT, SEM and HRXRD experiments has been conducted. SWBXT revealed single crystalline nature and determined the basic epitaxial relationships, which were found to be $(111)\langle\bar{1}\bar{1}2\rangle_{BP}\|(0001)\langle11\bar{2}0\rangle_{4H\text{-}SiC}$ with 4° off-axis towards $[1\bar{1}00]$ and $(111)\langle\bar{1}\bar{1}2\rangle_{BP}\|(0001)\langle1\bar{1}00\rangle_{4H\text{-}SiC}$ with 8° off-axis towards $[1\bar{1}00]$. BP twins were observed with a 180° (or equivalently 60°) rotation about surface normal. SEM and HRXRD both revealed better crystalline quality of 4° off $[1\bar{1}00]$ films compared with the 8° film. Peak intensity and the FWHM data indicated poor quality of the $(111)_{BP}\|(0001)_{4H\text{-}SiC}$ system. From high-precision mismatch calculations, the BP epitaxial growth was not completely relaxed through nucleation of dislocations, with high out-of-plane strain magnitude in the range of -19.146% ~ 0.933%. Concluded results showed that the 4H-SiC films with growth temperature of 1150 °C, P/B ratio of 10 and 4° off-axis substrate were preferred for growing higher quality films in this material system.

2.2 Introduction

Thick BP films were grown on c-plane 4H-SiC substrates using the CVD method. Among all of the SiC polytypes, 4H-SiC was selected because of its relative maturity of growth and good electronic properties. The (111) BP is three-folded structure, when growing on the six-fold 4H-SiC, the epitaxial twin structure is expected to form due to the atomic preference. Set BP as the reference, the theoretical lattice mismatch with respect to 4H-SiC is -4.074%. This lattice mismatch would induce large strains starting from the initial epitaxial growth, defects such as dislocations, twins and stacking faults would be present due to relaxation of the strains. Previous studies on $(0001)\langle1\bar{1}00\rangle_{B12As2}\|(0001)\langle1\bar{1}00\rangle_{4H\text{-}SiC}$ [14] indicate better crystalline quality on off-axis 4H-SiC compared with on-axis ones. Parameters such as off-cut orientation and magnitude, as well as growth parameters (temperature, P/B ratio, and growth time) will contribute to the film quality and device performance.

2.3 Experiment

BP films were deposited on 4H-SiC substrates using the chemical vapor deposition (CVD) technique. The CVD reactor consisted of a horizontal quartz tube cooled externally by a water jacket. Ultra-high purity gases of phosphine (99.999% PH_3) and diborane (1% B_2H_6 in H_2) were used as the precursor, with palladium membrane purified hydrogen as the carrier gas because of the high toxicity of B_2H_6 gas. Substrates were cleaned before heating on a TaC coated graphite susceptor with RF induction. Temperature was controlled by calibrating the thermocouple against the melting of a silicon piece on the susceptor. Films were deposited on two types of substrates: the (0001) 4H-SiC substrates with either 8° off or 4° off along $[1\bar{1}00]$ direction. Temperatures were varied from 1000 °C, 1100 °C and 1200 °C respectively, P/B ratio varied from 100, 150 and 200. Reaction time was set as 30 mins, 60 mins or 3 hours. All deposited films were performed at near atmospheric pressure (700 torr). Detailed information of all the samples is shown in Table. 2-1.

Table. 2-1 Sample information of BP grown on 4H-SiC substrates

Substrate	Sample #	Temperature (°C)	P/B ratio	Time
P-type 4H-SiC, 8°off-axis towards $[1\bar{1}00]$	141	1100	100	60 min
	45	1150	10	3 hour
	48	1150	10	3 hour
4H-SiC,	70	1250	100	3 hour
4°off-axis towards	152	1000	150	30 min
$[1\bar{1}00]$	153	1000		
	159	1100	200	30 min
	165	1200		

Basic epitaxial relationships, rotational twinning and the general film quality were determined using the SWBXT technique, which was conducted at Beamline X-19C, National Synchrotron Light Source (NSLS) at Brookhaven National Lab as well as 3.3.2 Advanced Light Source at Berkeley Lab. The white beam X-ray had wavelength spectrum ranging from 0.01Å to 2.00Å, in which the beam peak had a wavelength of 0.8 Å. The transmission geometry Laue patterns were recorded on STRUCTURIX D3-SC at a sample to film distance of 15 cm. Simulation of diffraction patterns was processed using the software LauePt. Surface morphology and grain size were analyzed through SEM at Stony Brook University.

High resolution X-ray rocking curve measurement was carried on the Bede D1 Diffractometer at Stony Brook University. The Ultima III Diffractometer at Center for Functional Nanomaterials at Brookhaven National Lab was used as assistance for the reciprocal space mapping. Samples were mounted vertically. In case of off-cut of substrate along $[1\bar{1}00]$, the off-cut direction and magnitude was determined by ω-relative scan of 4H-SiC, from which we make sure that the X-ray beam was accurately perpendicular to the (0001) surface of 4H-SiC substrate. Followed by the alignment procedure, rocking curves of ω-2θ as well as ω-relative BP were measured.

2.4 Results and discussion

2.4.1 SWBXT and SEM results

For SWBXT, both transmission and grazing incidence modes were applied, but grazing incidence topographs recorded from these layers were not able to effectively reveal detailed microstructure due to large strains inside the films. Exposure time of the transmission X-ray topography images was four minutes. Recorded images are shown in Fig. 2-1(a) and (b).

Combined with the laser alignment method, the epitaxial relationships were found to be $(111)<\bar{1}\bar{1}2>_{BP}||(0001)<11\bar{2}0>_{4H\text{-}SiC}$ with 4° off along $[1\bar{1}00]$ direction and $(111)<1\bar{1}0>_{BP}||(0001)<1\bar{1}00>_{4H\text{-}SiC}$ with 8° off along $[1\bar{1}00]$ direction. Diffraction patterns from the LauePt program confirmed the three-fold geometry of (111) BP and the six-fold geometry of (0001) 4H-SiC. In this case, twinned BP diffraction patterns comprised with 180° rotation about BP matrix were observed. It is easy to deduce that BP twins formed because of the natural atomic selection when a three-fold structure is grown on a six-fold structure. This defect structure will also be seen later in BP grown on 6H-SiC and AlN-buffered sapphire substrates. Transmission X-ray

topographs revealed general good crystalline quality of the BP||4H-SiC films. Compared with 4H-SiC diffraction spots which are more clear and intense, the diffraction intensity of BP is blurred and lighter. As indicated in the first chapter, the technique of growing high quality 4H-SiC wafer is much more mature, since the research on BP growth was only started in recent years.

Fig. 2-2 (a)(b) showed the selected SEM images recorded from sample 141 and 159. Better surface smoothness and smaller grain size were observed in the sample 159 with 4° off-cut along $[1\bar{1}00]$. This indicated off-cut angle of 4° is preferred for growing better BP||4H-SiC films. Fig. 2-2 (c)(d)(e) set temperature as the variation, and the results shows that BP grown under 1000°C showed amorphous surface, thus higher temperature (1200°C) is preferred since the surface smoothness is greatly improved. In addition, twins with the triangular feature were observed from SEM images, with a 180° (or equivalent 60°) rotation around the surface normal. Compared with BP||4H-SiC samples with reaction time of 3 hours, results indicate that shorter reaction time may help realizing better eptaxial quality.

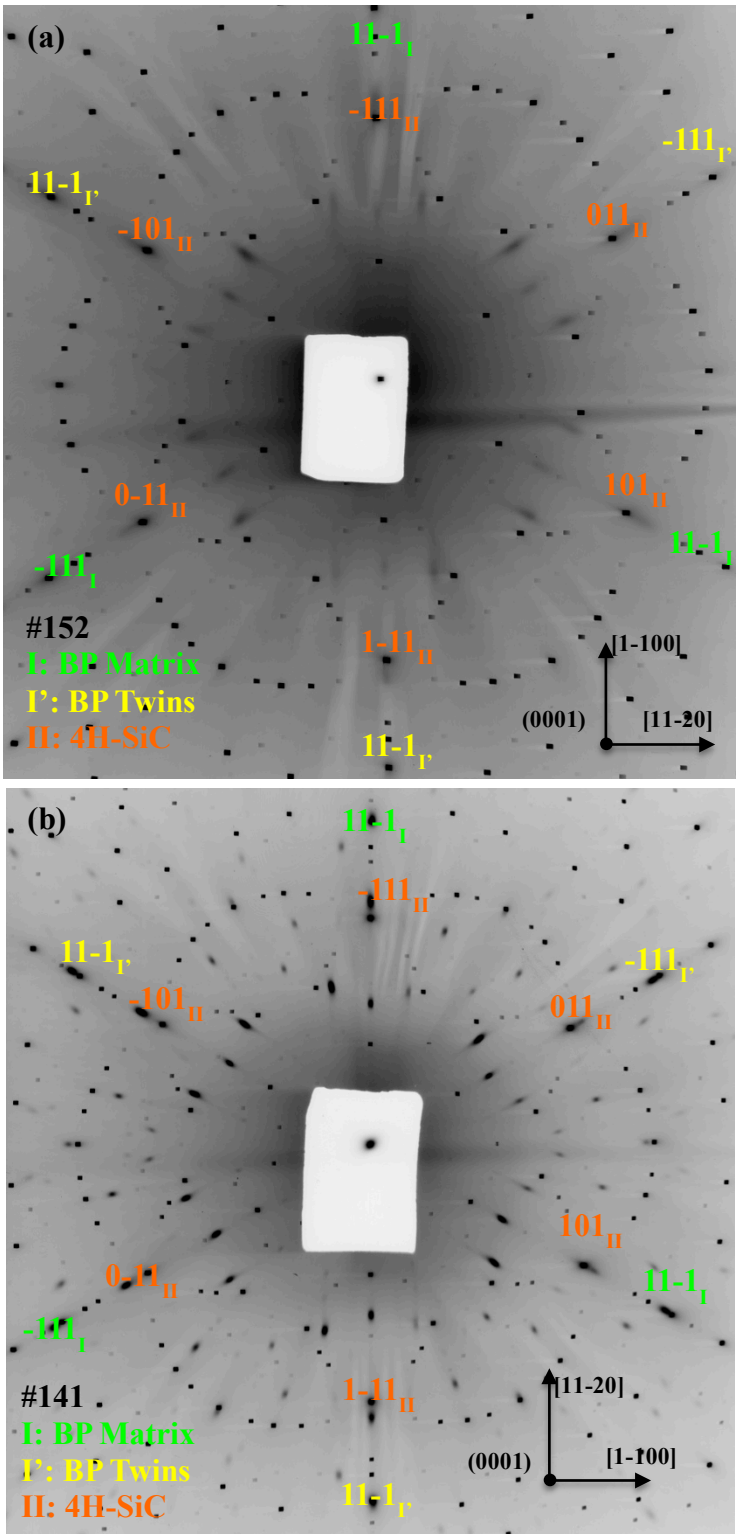

Fig. 2-1 Indexed transmission SWBXT image recorded from BP grown on 4H-SiC: (a) sample 152 (b) sample 141. BP matrix marked by green color, BP twins marked by yellow, substrate marked by orange.

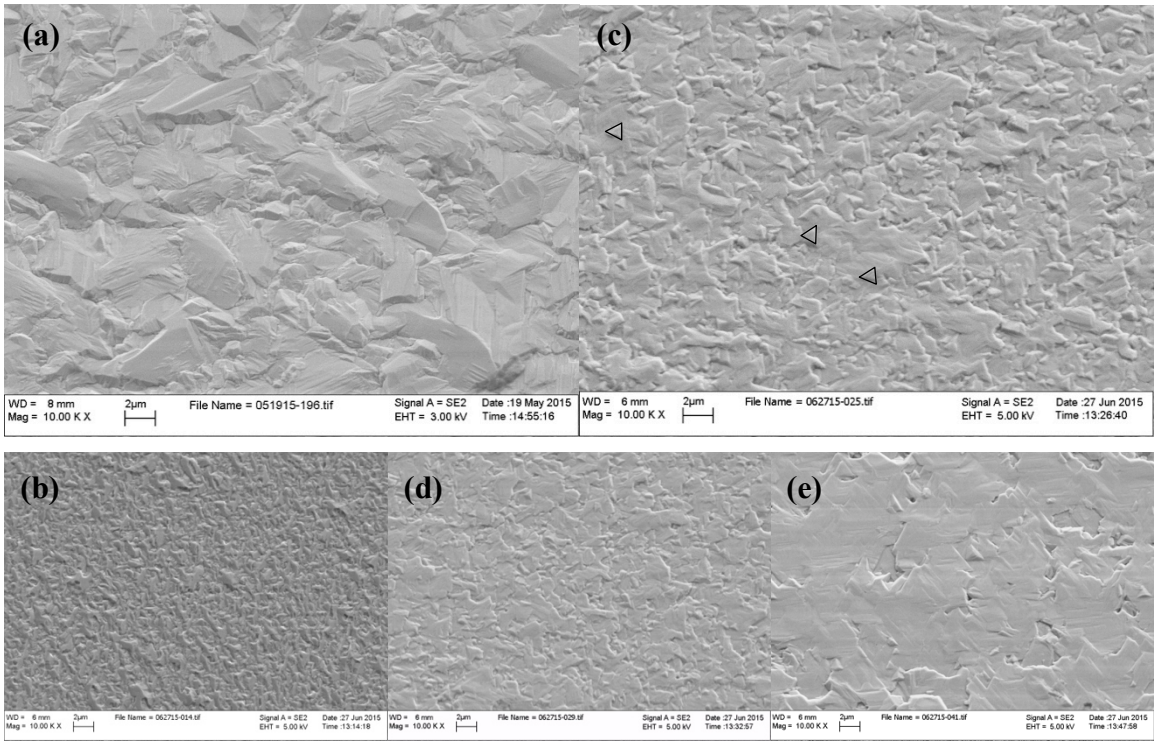

Fig. 2-2 SEM images of samples varied by off-cut magnitude: (a) 141 with 8° off-cut; (b) 152 with 4° off-cut; SEM image of samples varied by temperature: (c) 153 under 1000 °C; (d) 159 under 1100°C; (e) 165 under 1200°C.

2.4.2 HRXRD results

HRXRD results are shown in Fig. 2-3. Compared with all the rocking curve data, longer reaction time seems to increase the BP intensity as well as BP/4H-SiC ratio, but the increase in full width at half maximum (FWHM) value indicated poorer quality of the film. Generally, sample 45 with growth temperature 1150°, P/B = 10 was observed with best quality, its FWHM = 763.9 arc seconds and the intensity ratio BP/4H-SiC is larger than one. Compared with sample 153, 159 and 165, it is reasonable to deduce that higher temperature would boost the BP growth, but since the FWHM values are varied only by small amount, combined with SEM results, the favorable growth conditions for BP||4H-SiC is not conclusive.

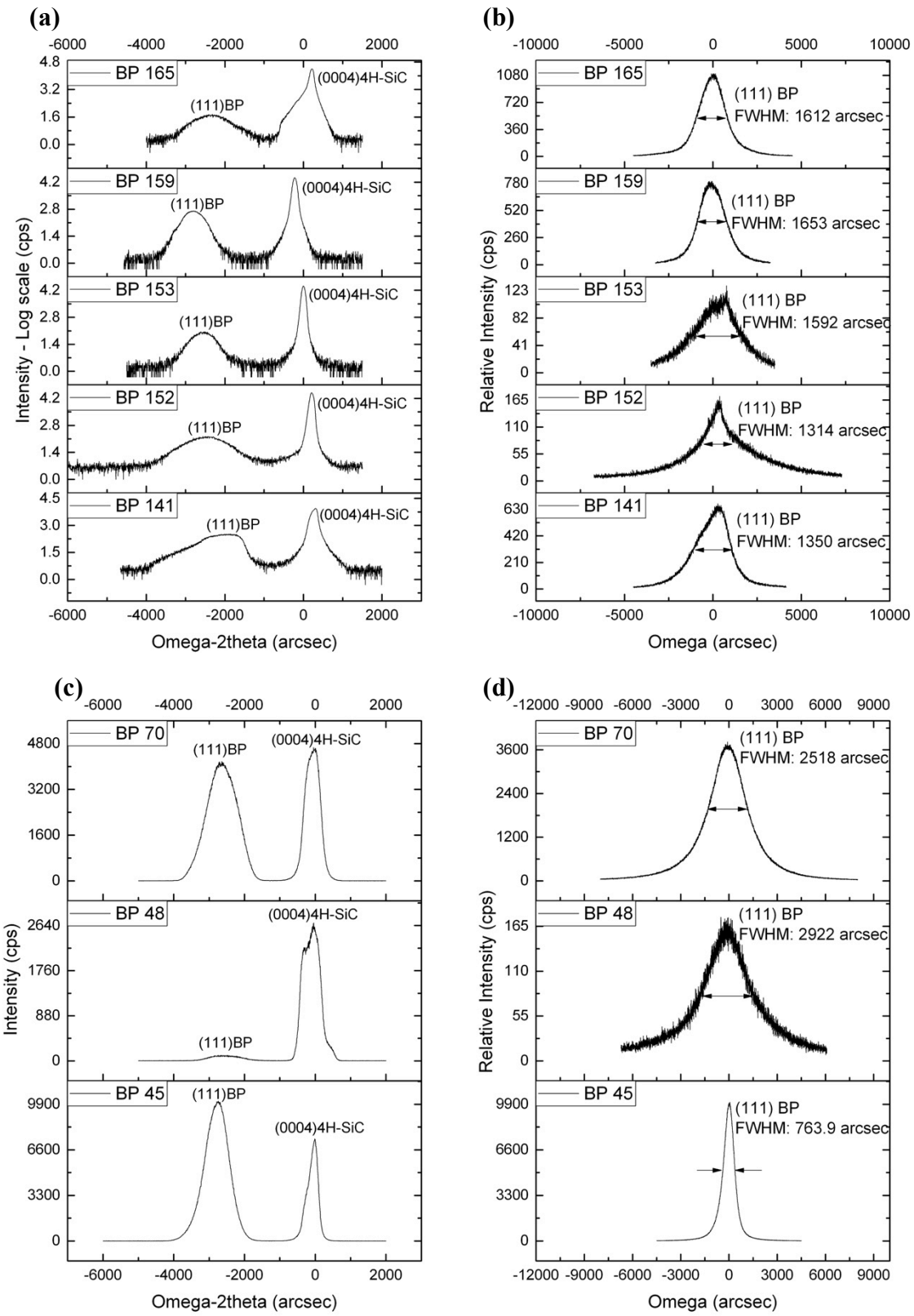

Fig. 2-3 HRXRD rocking curve measurements of BP grown on 4H-SiC substrates. (a)(c) ω-2θ scan (111) BP peak (left) and (0002) 4H-SiC (right), (b)(d) ω-relative scan of (111) BP

For a more precise comparison of the rocking curve width, the processed data are listed in the Table. 2-2.

Table. 2-2 Rocking curve data of BP grown on 4H-SiC substrates

Substrate	Sample #	Off-cut Magnitude By HRXRD	FWHM by ω - rel (arcsec)	FWHM from ω - 2θ (arcsec)	Theoretical Mismatch	Mismatch By ω - 2θ	Out-of-plane Strain
4H-SiC, 8° off-axis towards [1$\bar{1}$00]	141	8.082	4H-SiC: 121.7 BP: 1350	4H-SiC: 127.7 BP: 830.7		-3.294%	~ -19.146%
4H-SiC, 4° off-axis towards [1$\bar{1}$00]	45	3.803	4H-SiC: 266.3 BP: 763.9	4H-SiC: 330.9 BP: 793	-4.074%	-4.112%	~ -0.933%
	48	3.886	4H-SiC: 587.3 BP: 2922	4H-SiC: 609.1 BP: 946.2		-3.931%	~ -3.510%
	70	3.95	4H-SiC: 434.9 BP: 2518	4H-SiC: 513.5 BP: 968.9		-3.371%	~ -17.256%
	152	3.135	4H-SiC: 82.6 BP: 1314	4H-SiC: 105.3 BP: 851.5		-4.169%	~ -2.331%
	153	3.72°	4H-SiC: 94.53 BP: 1592	4H-SiC: 91.55 BP: 499.7		-3.786%	~ -7.069%
	159	4.11°	4H-SiC: 120.9 BP: 1653	4H-SiC: 103 BP: 462.7		-3.890%	~ -4.516%
	165	-4.48	4H-SiC: 142.3 BP: 1612	4H-SiC: 100.7 BP: 863.29		-4.876%	~ 19.686%

For BP grown on 4° off-axis 4H-SiC substrates, the deviation term is $\sqrt{\frac{|\gamma_h|}{\gamma_0}} \approx 0.802$, which indicates 19.8% of FWHM value comes from the asymmetrical reflection. For BP grown on 8° off-axis 4H-SiC substrate, the deviation term equals to $\sqrt{\frac{|\gamma_h|}{\gamma_0}} \approx 0.626$, and there is 37.4% deviation. In this case, the rocking curve measurement is not accurate and the asymmetrical scans should be performed for more accurate analysis.

The calculation results are shown in Table 2-2. The large out-of-plane strains in sample 141 (BP grown on 8° off 4H-SiC substrate) and 165 (BP grown on 4° off 4H-SiC substrate) indicate large strain at the interface, which means films were not relaxed during the growth. It is safe to conclude that 4° off-axis (0001) 4H-SiC would be better for BP epitaxial growth. But the sample 45 was almost relaxed with only -0.933% out-of-plane strain.

2.5 Conclusion

A combination of techniques have been applied for defect studies in $(111)_{BP}||(0001)_{4H\text{-}SiC}$ films. SWBXT has confirmed good single crystalline nature and the epitaxial relationships. BP rotational twins have been observed in both XRT and SEM. High resolution rocking curve measurements indicate poor quality of BP epitaxial layer compared with substrates, with high FWHM and large strains at the interface. In order to grow high quality BP for this system, results indicate that 4° off-axis (0001) 4H-SiC and higher temperature are favored parameters.

Chapter 3. Defect Studies of BP grown on C-plane Off-axis 6H-SiC Substrate

3.1 Outline

A detailed analysis of BP heteroepitaxial growth on c-plane 6H-SiC substrates is presented. SWBXT, SEM and HRXRD experiments have been conducted for analyzing film quality and defects. SWBXT confirmed the single crystalline nature and the epitaxial relationship was found to be on-axis $(111)\langle\bar{1}\bar{1}2\rangle_{BP}\|(0001)\langle11\bar{2}0\rangle_{6H\text{-}SiC}$ and $(111)\langle\bar{1}\bar{1}2\rangle_{BP}\|(0001)\langle11\bar{2}0\rangle_{6H\text{-}SiC}$ with 3.5° off-cut towards $[1\bar{1}00]$. Twins were observed from the diffraction patterns with a 180° (or equivalently 60°) rotation about [0001], and this was also corroborated by the SEM studies. High-resolution rocking curve measurements revealed increased FWHM values compared with 4H-SiC films, especially under high temperatures. Lattice mismatch calculation results indicate highly strained interface in all the samples.

3.2 Introduction

Beside 4H-SiC, 6H-SiC growth has been investigated for a long period of time, so that it is selected for growing BP thin films for better quality as is expected. Chemical vapor deposition (CVD) technique was applied for BP deposition on off-axis 6H-SiC substrates. Previous studies of $B_{12}As_2$ films indicated better crystalline quality when the 6H-SiC was off-cut by 3.5° along $[1\bar{1}00]$ direction. [15] In this study, on-axis 6H-SiC was set as comparison with off-axis 6H-SiC substrates for BP epitaxy. Similar to 4H-SiC, BP twins were formed during growth on 6H-SiC substrates. Theoretical lattice mismatch along [0001] is -3.881%, this mismatch would induce strains at the interface region, from which defects such as dislocations and stacking faults can be generated as relaxation effects.

3.3 Experiment

BP films were deposited on 6H-SiC substrates using CVD technique. The CVD reactor consisted of a horizontal quartz tube cooled externally by a water jacket. Ultra-high purity gases of phosphine (99.999% PH_3) and diborane (1% B_2H_6 in H_2) were used as the precursor, with palladium membrane purified hydrogen as the carrier gas. Substrates were cleaned before heating on a TaC coated graphite susceptor with RF induction. Temperature was controlled by calibrating the thermocouple against the melting of a silicon piece on the susceptor, which varied from 1150 °C, 1200 °C and 1250 °C. Samples were deposited on the (0001) 6H-SiC substrates with both on-axis and with 3.5° off-cut along $[1\bar{1}00]$ direction. P/B ratios selected were 10, 100 or 1000. Reaction time was set as 30 mins, 60 mins or 90 mins. All deposited films were performed at near atmospheric pressure (700 torr). Detailed information of the samples is shown in Table. 3-1.

Table. 3-1 Sample information of BP grown on 6H-SiC substrates

Substrate	Sample #	Temperature (^{o}C)	P/B ratio	Time
P-type 6H-SiC,	137	1200	100	60 min
3.5^{o} off-axis towards	46	1150	10	30 min
$[1\bar{1}00]$	61	1250	1000	90 min
C-plane 6H-SiC,	47	1150	10	30 min
on-axis				

Basic epitaxial relationships, rotational twinning and the general film quality were determined by the synchrotron white beam X-ray topography technique, which was conducted at the National Synchrotron Light Source (NSLS) at Brookhaven National Lab. The white beam X-ray had wavelength spectrum ranging from 0.2Å to 2.00Å, with peak beam intensity at 0.8 Å. The transmission geometry Laue patterns were recorded on STRUCTURIX D3-SC X-ray films at a sample to film distance of 15cm. Simulation of diffraction patterns was processed using the software LauePt. Surface morphology and grain size were analyzed through scanning electron microscopy (SEM) at Stony Brook University.

High resolution X-ray rocking curve measurement was carried on the Bede D1 Diffractometer at Stony Brook University. The Ultima III Diffractometer at Center for Functional Nanomaterials at Brookhaven National Lab was used as assistance for the reciprocal space mapping. Samples were mounted vertically. In case of off-axis substrates along certain direction, the off-cut direction and magnitude was determined by ω-relative scan of 6H-SiC, from which the X-ray beam would be accurately perpendicular to the (0001) surface of 4H-SiC substrate. For on-axis samples, mounting direction would not make any difference. Following the alignment procedure, rocking curves of ω-2θ as well as ω-relative BP were measured.

3.4 Results and discussion

3.4.1 SWBXT and SEM results

Both the transmission and grazing incidence X-ray topography were applied. However, defect microstructures could not be discerned due to the large strains inside the film. Transmission X-ray topography (Fig. 3-1) confirmed the single crystalline nature, with strong six-fold diffraction patterns from the 6H-SiC and the three-fold BP with a 180° twinned structure. Compared with substrate, Laue patterns from BP were blurred and lighter, indicating the poor quality of the film. From LauePt program, some of the blurred patterns could not be matched well with both BP and 6H-SiC.

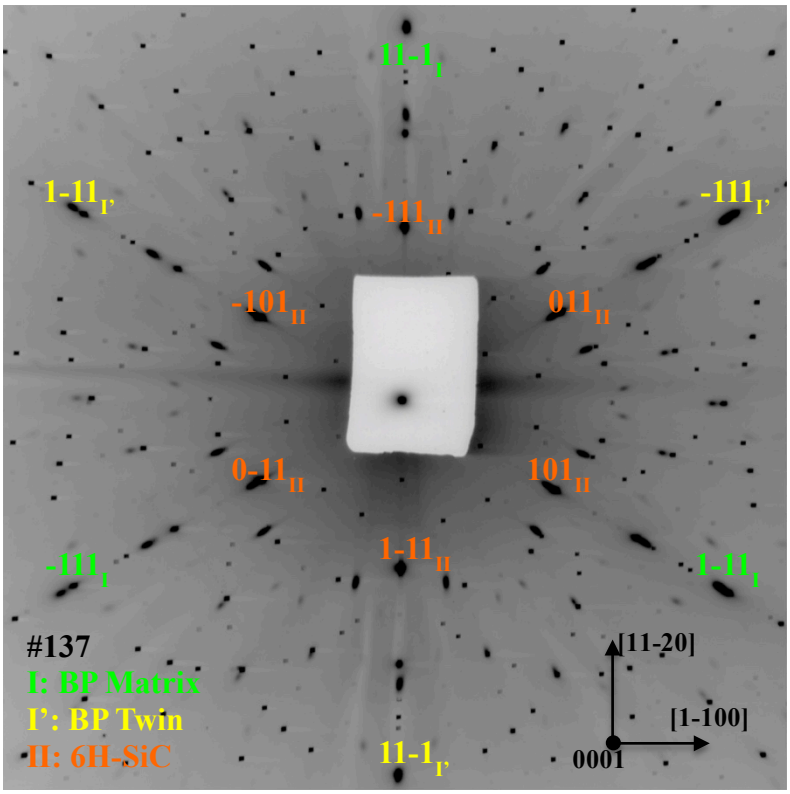

Fig. 3-1 Indexed transmission topography recorded from BP grown on 6H-SiC substrate with 3.5° off-cut towards [1$\bar{1}$00]. Green: BP matrix, yellow: BP twins, orange: 6H-SiC substrate

Laser alignment technique was applied for more precise measurement of off-cut magnitude and direction. Basic epitaxial relationships of the films were found to be (111)<$\bar{1}\bar{1}$2>$_{BP}$|| (0001) <11$\bar{2}$0>$_{6H\text{-}SiC}$ and (111)<$\bar{1}\bar{1}$2>$_{BP}$||(0001)<11$\bar{2}$0>$_{6H\text{-}SiC}$ with 3.5° off-cut towards [1$\bar{1}$00].

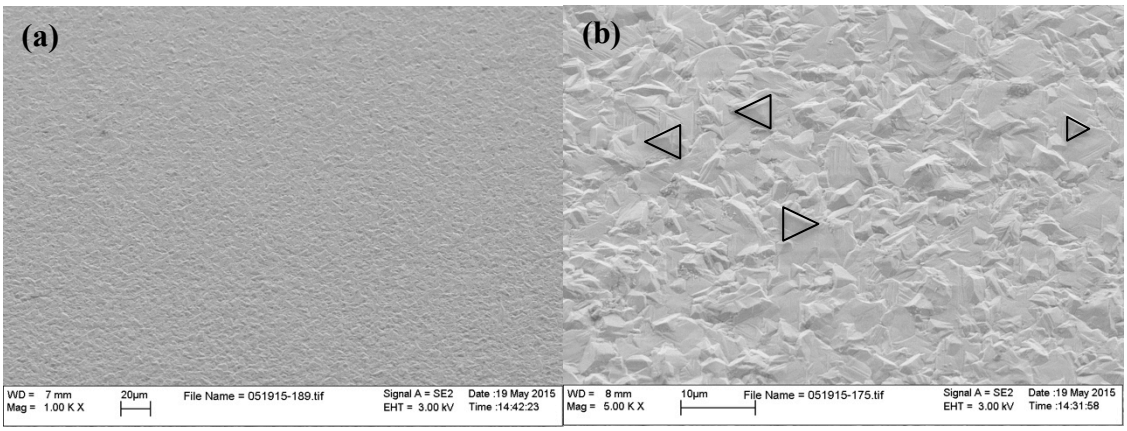

Fig. 3-2 SEM images of BP grown on 6H-SiC substrate (a) exposed under 20 µm (b) exposed under 10 µm, triangular twins are marked in black

SEM images can be seen from Fig. 3-2 (a)(b). BP||6H-SiC films showed clean surface without extra growth under low magnification. Under higher magnification, twins grown with the triangular feature with a 180° difference were observed, which confirmed the previous SWBXT results.

3.4.2 HRXRD results

HRXRD results are shown in Fig. 3-4. Combine the ω - 2θ and the ω-relative scan of (111) BP, it has been found that sample 46 has highest intensity ratio of BP: 6H-SiC. But still, the FWHM value of (111) BP indicated its poor quality compared with sample 45 (BP||4H-SiC) which was discussed in chapter 2. On the other hand, when we focused on the substrate material, the 6H-SiC peaks showed high intensity but peak split was observed in two samples, probably due to the low angle grain boundaries in the substrate. Thus, we concluded that 4H-SiC might be a more suitable choice of growing (111) BP epilayer. But generally, from a comparison of all the BP||6H-SiC films, favored growth parameters are 1100°C, P/B = 10, and reaction time of 30 minutes.

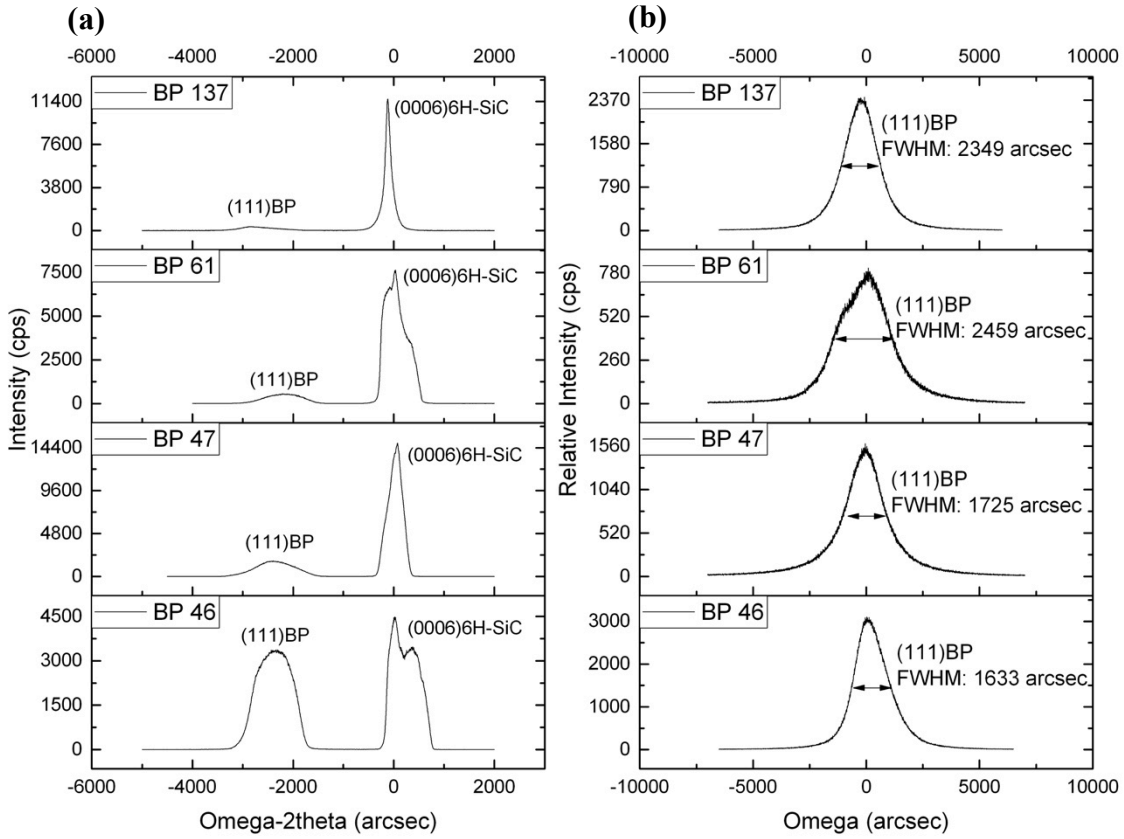

Fig. 3-3 High-resolution rocking curves of BP grown on 6H-SiC. (a): ω - 2θ scan, left (111) BP peak, right: (0006) 6H-SiC peak, (b): ω-relative scan of (111) BP

For a clearer comparison of FWHM, the processed data are listed in Table. 3-2.

Table. 3-2 HRXRD results from BP grown on 6H-SiC substrates

Substrate	Sample #	Off-cut by HRXRD	FWHM ω - rel (arcsec)	FWHM ω - 2θ (arcsec)	Theoretical Mismatch	Mismatch by ω - 2θ	Out-of-plane Strain
(0001) 6H-SiC, On-axis	47	-	6H-SiC: 351.4 BP: 1725	6H-SiC: 333.7 BP: 877.3		-3.688%	~ -4.973%
P type (0001) 6H-SiC, 3.5° off-axis towards [1$\bar{1}$00]	137	3.428	6H-SiC: 197.9 BP: 2349	6H-SiC: 160.3 BP: 926.4		-3.763%	~ -3.040%
	46	5.11	6H-SiC: 1156 BP: 1633	6H-SiC: 723.9 BP: 740	-3.881%	-3.634%	~ -6.364%
	61	3.644	6H-SiC: 1982.9 BP: 2549	6H-SiC: 504.2 BP: 801.6		-3.393%	~ -12.574%

As mentioned in the previous section, the rocking curves were measured from c direction. Thus for 6H-SiC substrates with off-axis polishing, the deviation term should be added for a more precise calculation of FWHM. The deviation term for 6H-SiC with 3.5° off-cut is: $\sqrt{\frac{|\gamma_h|}{\gamma_0}} \approx 0.825$. This indicates that measured FWHM values are lower than corresponding symmetrical reflection by 17.5%.

Using the same method, the high-precision lattice mismatch were calculated, which is shown in Table. 3-2. From the results, all of the films contain certain amount of strain at the interface. Sample 61 contains the largest strain, combining the FWHM value of BP, it is concluded that higher temperature and P/B ratio are not favorable conditions for BP epitaxial growth on 6H-SiC substrates.

3.5 Conclusion

A series of experiments have been conducted for defect studies in $(111)_{BP}||(0001)_{6H\text{-}SiC}$ films. SWBXT indicated good single crystalline nature and confirmed the epitaxial relationships of both on-axis and off-axis samples. Rotational BP twins were observed from XRT and SEM. High resolution rocking curves indicate poor quality of BP compared with 6H-SiC, with strains at the interface that varied from each sample. For more accurate studies on how growth parameters would influence the film quality, more comparison groups should be included.

Chapter 4. Defect Studies of CVD Grown BP Epilayers on 3C-SiC/Si Substrates

4.1 Outline

A detailed analysis of the crystalline quality and structure in BP epitaxial growth on 3C-SiC substrates is presented. SWBXT, SEM, HRXRD and TEM experiments were conducted as a combination. The X-ray topographs revealed single crystalline nature. Diffraction intensity of (100) BP and (100) 3C-SiC were both strong, which indicated good quality of the film. Basic epitaxial relationships were found to be $(100)\langle 011\rangle_{BP}\|\ (100)\langle 011\rangle_{3C\text{-}SiC}$ and $(111)\langle \bar{1}\bar{1}2\rangle_{BP}\|\ (111)\langle \bar{1}\bar{1}2\rangle_{3C\text{-}SiC}$, and no rotational twins of BP were observed. SEM and HRXRD studies both indicated desired quality of $(100)_{BP}\|\ (100)_{3C\text{-}SiC}$ film. Extensive high-precision measurements of relative out-of-plane lattice mismatch have been conducted, and the $(100)_{BP}\|(100)_{3C\text{-}SiC}$ heterofilms were found to be almost relaxed through the strain-induced defects (out-of-plane strain: -0.203%). Reciprocal space mapping (RSM) suggested that there was no rotational misorientation in the films. TEM studies on $(100)_{BP}\|(100)_{3C\text{-}SiC}$ confirmed the existence of $B_{12}P_2$ and its twins, dislocations and stacking faults. Smooth atomic connection was observed at the interface region, without any intermediate layer or second phase. All the results indicate good crystalline quality of $(100)_{BP}\|(100)_{3C\text{-}SiC}$ and can be potentially applied to devices.

4.2 Introduction

Thick BP films were deposited on 3C-SiC with (100) and (111) surfaces by CVD method. Compared with 4H-SiC and 6H-SiC, 3C-SiC possesses same structure, similar lattice parameter and thermal expansion coefficient with BP, which make it a desired substrate material for BP epitaxial growth. 3C-SiC was investigated only from recent years, because of the relative immaturity of growth and to increase its stability, 3C-SiC is commonly grown as the buffer layer on Si substrates (written as 3C-SiC/Si). Since more attention is being paid on epilayer growth, we do not focus on Si substrate and its interface with 3C-SiC. Set BP as reference, the lattice mismatch between BP and 3C-SiC is -3.938%, which is smaller compared with other SiC polytypes, but still create strains at the interface as the film grows. Variables in this system include the growth orientation [100] and [111], growth parameters such as temperature, P/B ratio and reaction time.

4.3 Experiment

Chemical vapor deposition technique was applied for the growth of BP||3C-SiC/Si. The CVD reactor consisted of a horizontal quartz tube cooled externally by a water jacket. Ultra-high purity gases of phosphine (99.999% PH_3) and diborane (1% B_2H_6 in H_2) were used as the precursor, with palladium membrane purified hydrogen as the carrier gas because of the high toxicity of B_2H_6 gas. Substrates were cleaned before heating on a TaC coated graphite susceptor with RF induction. Temperature was controlled by calibrating the thermocouple against the melting of a silicon piece on the susceptor. Films were deposited on two types of substrates: (100) 3C-SiC/Si and (111) 3C-SiC. Temperatures varied from 1000 °C to 1100 °C. P/B ratios were set as 100 and 150. Reaction time was set as 30 mins and 60 mins. All deposited films were performed at near atmospheric pressure (700 torr). Detailed information of the samples are shown in Table. 4-1.

Table. 4-1 Sample information of BP grown on 3C-SiC/Si

Substrate	Sample #	Temperature (°C)	PH_3/B_2H_6 (sccm)	P/B Ratio	Time
(100) 3C-SiC/Si	145	1000	40/40	100	30 min
(111) 3C-SiC/Si	146				
	129	1000	40/26.7	150	30 min
(100) 3C-SiC/Si	169				
	109	1100	40/40	100	60 min

Basic epitaxial relationships and the general film quality were determined using the SWBXT technique, which was conducted at Beamline X-19C, National Synchrotron Light Source at Brookhaven National Lab as well as 1-BM, Advanced Photon Source at Argonne National Laboratory. The white beam X-ray had wavelength spectrum ranging from 0.05Å to 2.00Å, with peak beam intensity at 0.8 Å. The transmission Laue patterns were recorded on STRUCTURIX D3-SC X-ray films at a sample to film distance of 15 cm. Simulation of diffraction patterns were processed using the software LauePt. Surface morphology and rough grain size were analyzed through SEM at Stony Brook University.

High resolution X-ray rocking curve measurement was carried on the Bede D1 Diffractometer at Stony Brook University. The Ultima III Diffractometer at Center for Functional Nanomaterials at Brookhaven National Lab was used as assistance for the reciprocal space mapping. Samples were mounted vertically. Since all the 3C-SiC substrates are on-axis, the alignment process can be omitted. Rocking curves of ω-2θ as well as ω-relative of BP were measured.

The TEM samples were prepared using the focused ion beam (FIB) technique, and TEM experiments were performed on JOEL2100F TEM system at Center for Functional Nano materials at Brookhaven National Lab.

4.4 Results and discussion

4.4.1 SWBXT and SEM results

The grazing incidence X-ray topography was not effective for microstructure analysis due to the expected high strains inside the film so that only transmission X-ray topography was applied. Topographs of both (100) BP and (111) BP films were recorded. Exposure time of the transmission X-ray topography images was four minutes.

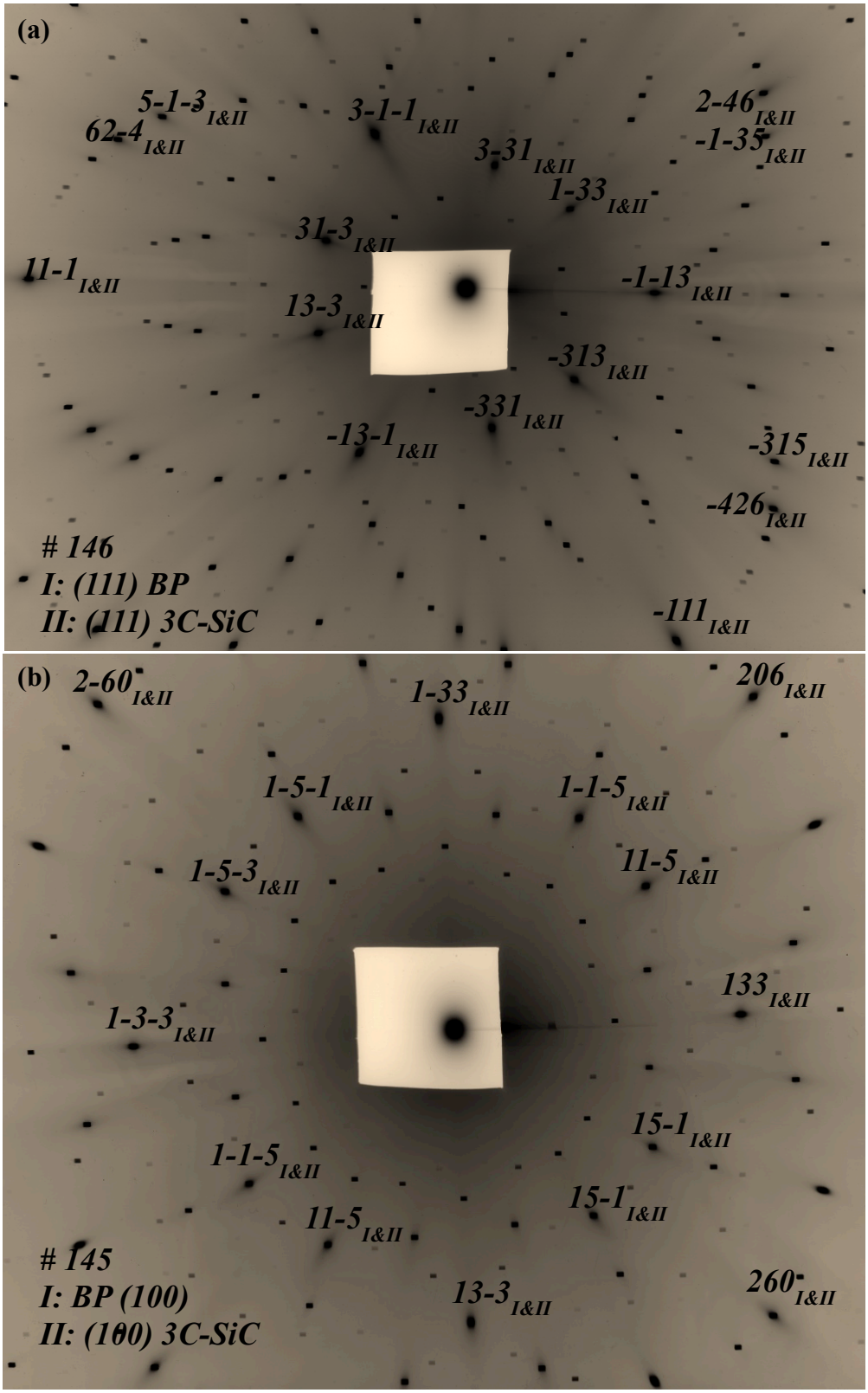

Fig. 4-1 Indexed transmission SWBXT Laue patterns recorded from BP grown on 3C-SiC buffered substrates. Diffraction patterns of both BP and 3C-SiC are overlapped, (a) I: (111) BP, II: (111) 3C-SiC, (b) I: (100) BP, II: (111) 3C-SiC

Indexed transmission topographs of two orientations are shown in Fig. 4-1. Diffraction patterns of the epilayer and the buffer were overlapped, with a three-fold structure in (111) surface and four-fold structure in (100). No twins were found related to the BP epitaxial structure. SWBXT confirmed the single crystalline nature. Also, the strong, well-shaped diffraction patterns of (100) BP indicated good quality of the $(100)_{BP}||(100)_{3C\text{-}SiC}$ films. Basic epitaxial relationships were found to be $(100)\langle 011\rangle_{BP}||\ (100)\langle 011\rangle_{3C\text{-}SiC}$ and $(111)\langle \bar{1}\bar{1}2\rangle_{BP}||(111)\langle \bar{1}\bar{1}2\rangle_{3C\text{-}SiC}$, without off-axis polishing in the 3C-SiC buffer.

SEM experiment was performed for surface morphology analysis. As indicated from the images in Fig. 4-2, $(100)_{BP}||(100)_{3C\text{-}SiC}$ films achieved a general high quality, with smoother surfaces and smaller grain size. Among all the samples grown along [100] direction, sample 145 tended to be the best, which indicated that lower temperature and higher diborane (B_2H_6) gas were the preferred growth parameters. For BP grown on (111) 3C-SiC/Si substrates, the densely distributed small pyramid structures with slight variations indicated the three-fold symmetry of (111) planes. But poor smoothness would influence the electronic properties such as conductivity, which would not be desired for device applications.

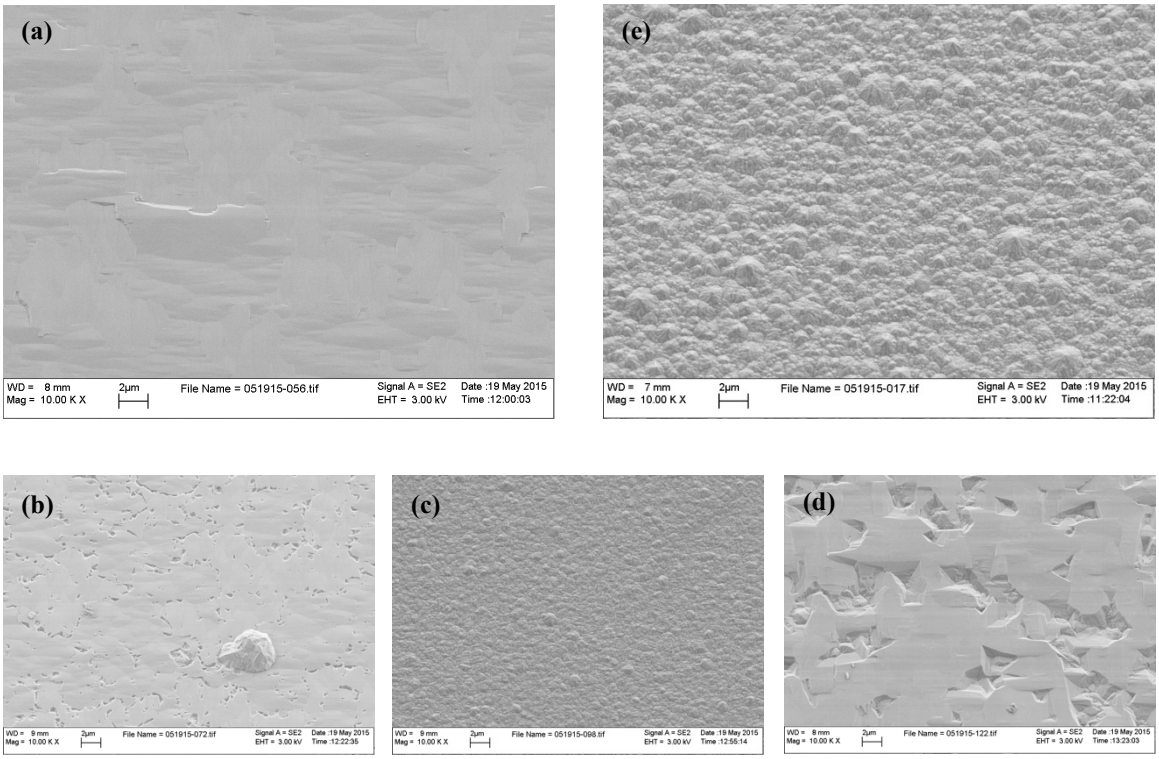

Fig. 4-2 SEM images recorded from BP grown on 3C-SiC substrates, (a) #145 $(100)_{BP}||(100)_{3C\text{-}SiC/Si}$, (b) #129 $(100)_{BP}||(100)_{3C\text{-}SiC/Si}$ (c) #169 $(100)_{BP}||(100)_{3C\text{-}SiC/Si}$, (d) #109 $(100)_{BP}||(100)_{3C\text{-}SiC/Si}$,(e) #146 $(111)_{BP}||(111)_{3C\text{-}SiC/Si}$

4.4.2 HRXRD Results

HRXRD rocking curves are seen in Fig. 4-3.

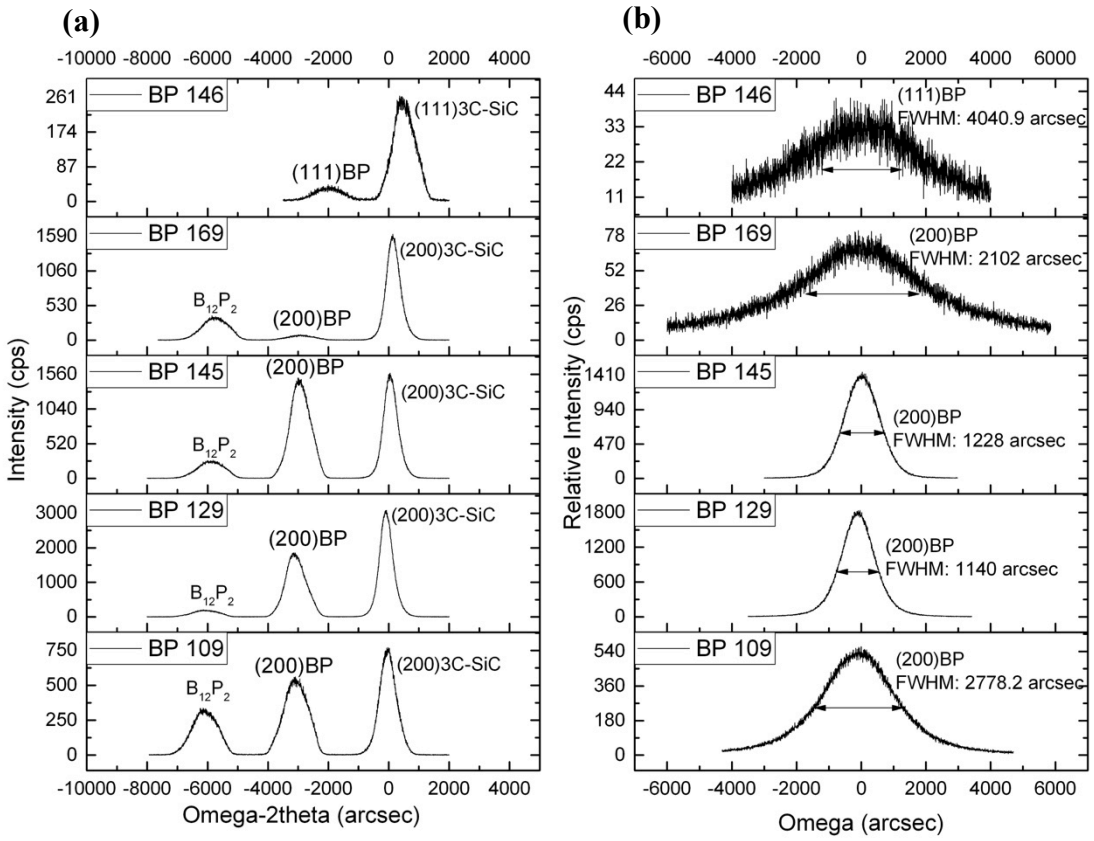

Fig. 4-3 High resolution X-ray rocking curves of BP grown on 3C-SiC buffered Si substrates. (a): ω - 2θ scans, the left peak indicates existence of $B_{12}P_2$, middle peak: (200) BP, right peak: (200) 3C-SiC (b): ω - relative scans of BP

Compare the results from $(100)_{BP}||(100)_{3C\text{-}SiC}$ and $(111)_{BP}||(111)_{3C\text{-}SiC}$, it was obvious that $(100)_{BP}||(100)_{3C\text{-}SiC}$ films possessed much better quality, especially for sample 145, with peak intensity ratio BP/3C-SiC ≈ 1. This observation also corroborated the SEM and SWBXT results. It is concluded that preferable growth conditions of the BP||3C-SiC system are: growth direction of [100], temperature 1000°C, P/B ratio 100 and 30-minute reaction time.

One interesting observation was that there is a third peak located left of (200) BP peak, with the diffraction intensity that could not be eliminated. Under increased temperature and longer reaction time, the relative intensity of this peak was increased. As indicated in the introduction part, this peak has high possibility of being $B_{12}P_2$. To avoid this defect structure, growth temperature should be controlled to avoid higher temperature for BP decomposition. Based on the peak position, lattice mismatch between the third peak and 3C-SiC was calculated and the results were compared with possible structures such as BN, BC_4, $B_{12}P_2$, SiB_3, SiP. Results indicated that the (0001) $B_{12}P_2$ has highest possibility, but still needed further technical evidence.

Table. 4-2 HRXRD data of BP grown on 3C-SiC/Si substrates

Sample #	Substrate	FWHM by ω-rel (arcsec)	FWHM by ω - 2θ	Theoretical Mismatch	Mismatch by HRXRD	Out-of-plane Strain
#145	3C-SiC/Si (100)	3C-SiC: 601.2	3C-SiC: 512.3		-3.930%	-0.203%
		BP: 1228	BP: 760.9			
		$B_{12}P_2$: 12193	$B_{12}P_2$: 967.266			
#146	3C-SiC/Si (111)	3C-SiC: 1135	3C-SiC: 760.2		-3.593%	-8.761%
		BP: 4040.9	BP: 1087.7			
#129		3C-SiC: 518.1	3C-SiC: 491.4		-3.950%	-0.305%
		BP: 1140	BP: 748.3			
		$B_{12}P_2$: 11543	$B_{12}P_2$: 965.5			
#169	3C-SiC/Si (100)	3C-SiC: 619.5	3C-SiC: 500.4	-3.938%	-3.924%	-0.356%
		BP: 2102	BP: 972.34			
		$B_{12}P_2$: 17083.7	$B_{12}P_2$: 981.3			
#109		3C-SiC: 692	3C-SiC: 603.9		-3.955	-0.432%
		BP: 2788.2	BP: 949.1			
		$B_{12}P_2$: 16832.1	$B_{12}P_2$: 963.8			

The rocking curve width of BP||3C-SiC was closer to the asymmetrical reflection since all the 3C-SiC buffer layers were on-axis so that the deviation term $\sqrt{\frac{|\gamma_h|}{\gamma_0}} = 1$. All the mismatch values as mentioned in 4H-SiC section, were calculated based on the symmetrical reflection. From Table. 4-2, the experimental lattice mismatch and strains indicate that the $(100)_{BP}||(100)_{3C\text{-}SiC}$ films were almost relaxed, with strain magnitude below 0.432%. Combine all the previous results together, it is concluded that (100) growth surface is favored for the BP||3C-SiC/Si system, and the film quality was much better than BP grown on 4H-SiC and 6H-SiC substrates.

4.4.3 TEM results

We selected sample 145 for TEM studies at Center for Functional Nanomaterials at BNL, since this sample possesses best quality among all the $(100)_{BP}||(100)_{3C\text{-}SiC}$ films. The TEM specimen was successfully prepared using FIB. The growth mechanism was easy to understand. As indicated by Fig. 4-4, both 3C-SiC and BP possess zinc blende structure, with very close lattice parameter (BP: a = 4.5383 Å; 3C-SiC: a = 4.3596 Å). Therefore, (100) BP is expected to sit on top of (100) 3C-SiC, with B on Si atoms and P on C atoms respectively.

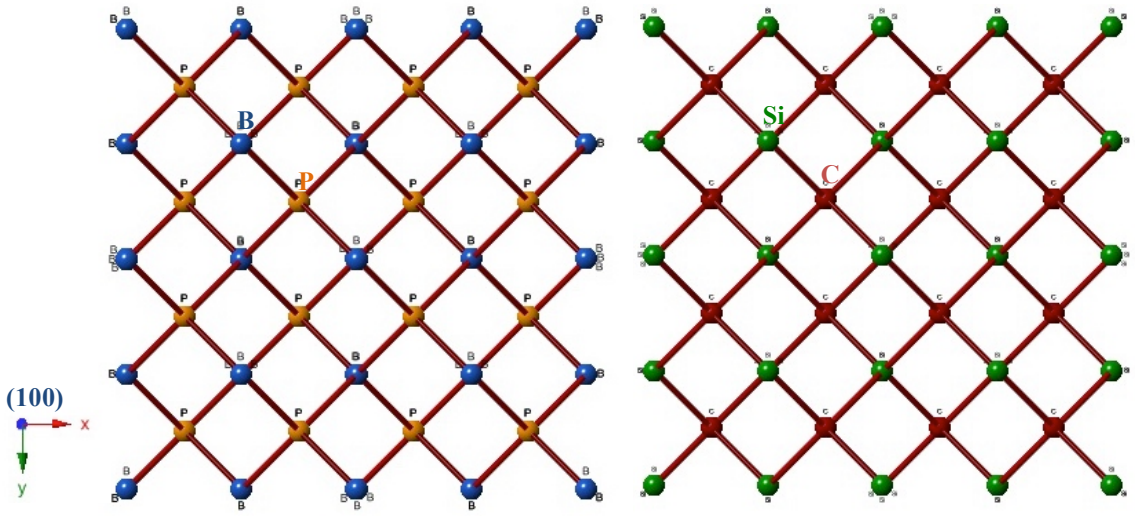

Fig. 4-4 Plan view of atomic stacking of left: (100) BP and right: (100) 3C-SiC

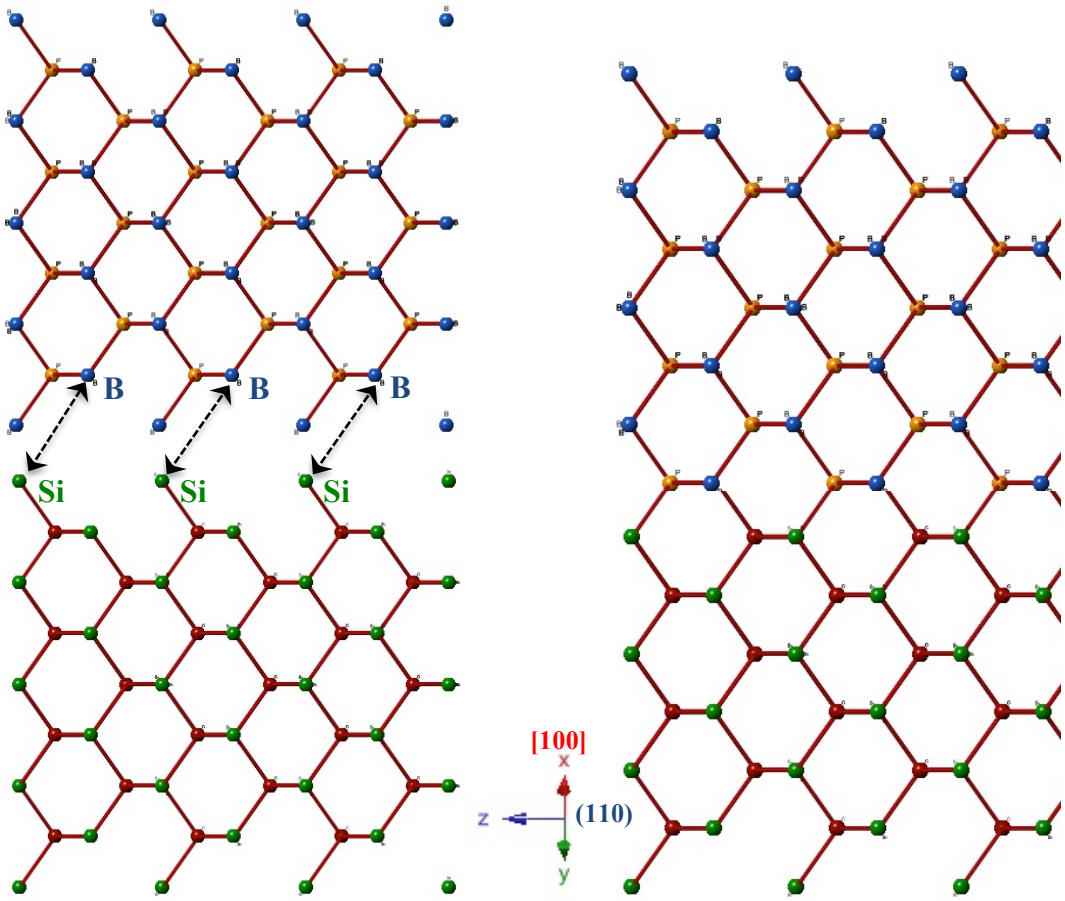

Fig. 4-5 Cross sectional view of atomic stacking before (left) and after (right) (100) BP growth on (100) 3C-SiC buffer layer. Smooth atomic connection is expected with both materials with same structure and close lattice parameter

Cross sectional low magnification TEM images were taken for a general view of the specimen and are shown in Fig. 4-6(a)(b). From the images, the 3C-SiC buffer layer was found to have pretty good crystalline structure with low density of dislocation lines. All the dislocations were ended at the interface. However, the initial growth of (100) BP showed poor quality, with high density of defects such as dislocations and stacking faults. But as the film grew to above 300 nm, the quality became better.

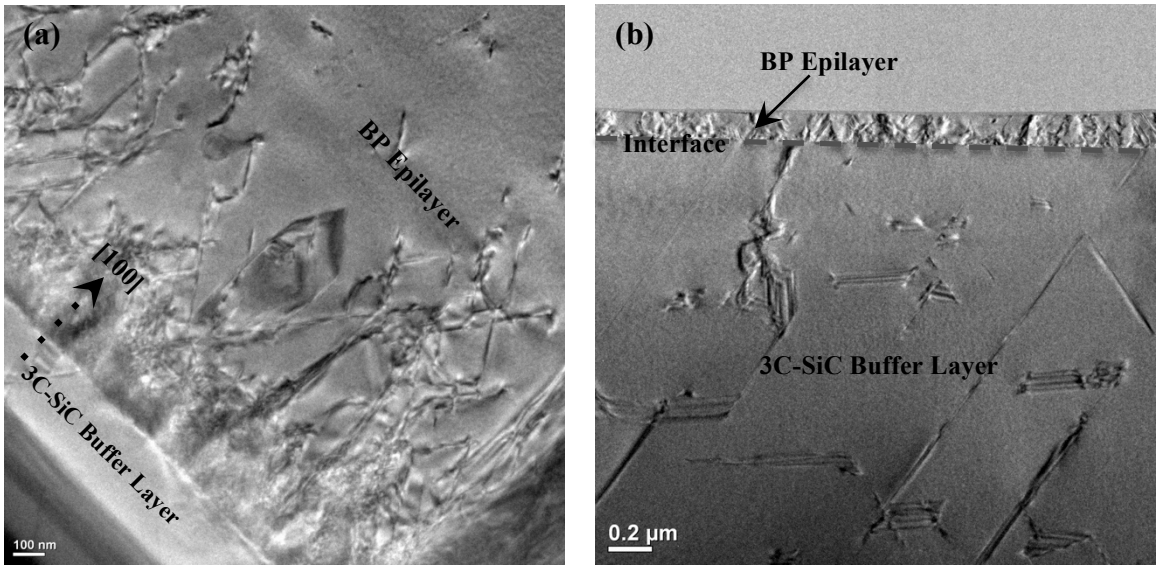

Fig. 4-6 Cross-sectional low magnification TEM images of (100) BP grown on (100) 3C-SiC buffer. (a) General film quality, exposed under 12K. (b) Exposed under 8K (part of the epilayer was cut by ion beam for better interface observation under HRTEM)

Selected area diffraction (SAD) patterns were taken with respect to the upper epilayer, near interface region and the 3C-SiC buffer, and the results are shown in Fig. 4-7. Diffraction patterns taken at 3C-SiC buffer indicated single crystalline nature and good quality. However, moving to the interface region, diffraction patterns (DPs) showed a second phase besides (110) BP. When exposed under longer time, the twinned DPs of this second phase were observed as well. As indicated in HRXRD results, this second phase has high possibility of being the boron subphosphide ($B_{12}P_2$).

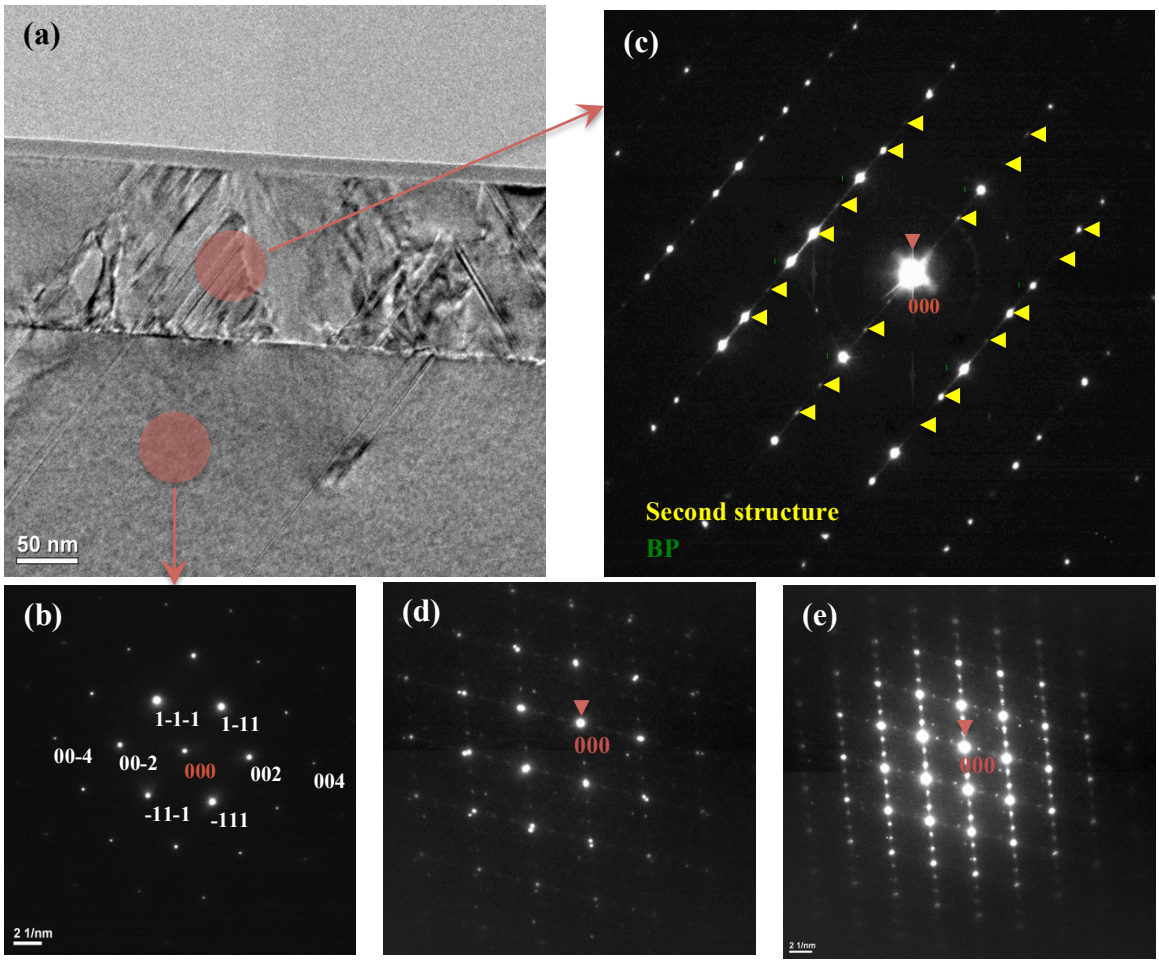

Fig. 4-7 Selected area diffraction (SAD) patterns recorded from 3C-SiC buffer and near interface region of the BP epilayer. (a) Low magnification image of the interface. (b) Indexed SAD patterns recorded from 3C-SiC buffer layer, (c)-(e) SAD patterns recorded in the initial growth region which indicates a second phase and its twins

HRTEM experiments were carried to study the microstructure at the interface. Since the BP epilayer was grown to be thick, a large part of the epilayer was cut using the ion beam, so that the atomic stacking at the interface was obtained successfully. Fig. 4-8(a)-(c) shows the high-resolution image taken at the interface. Compare the atomic stacking with the simulated model, smooth atomic connection was observed, without obvious phase or the transition layer.

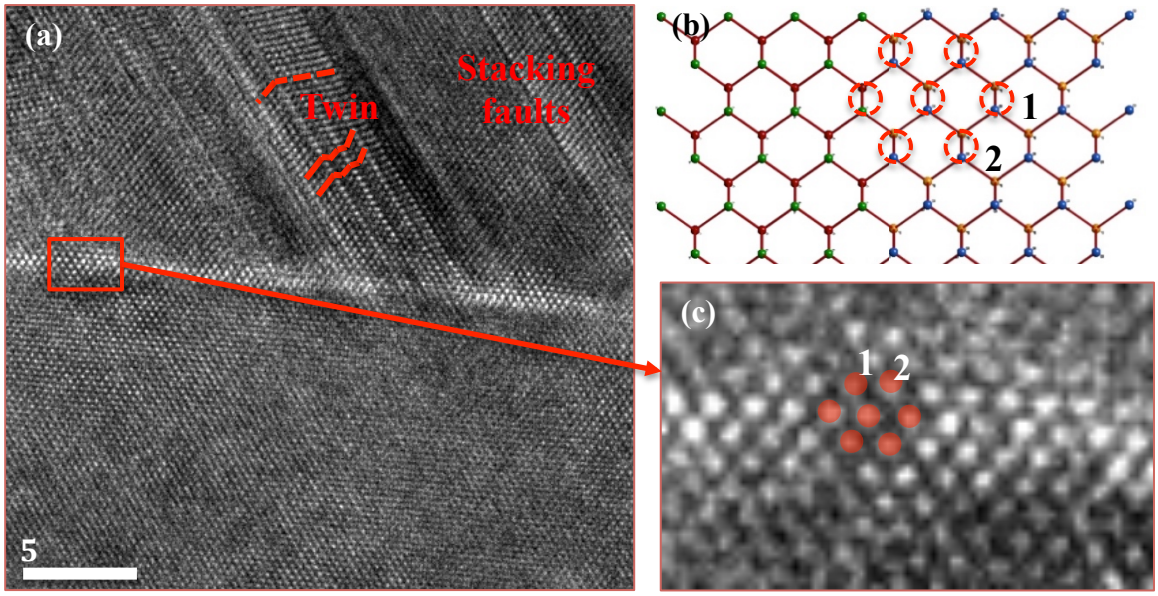

Fig. 4-8 (a) HRTEM image at the interface region, twins and stacking are marked in read. (b) Simulated HRTEM image at interface, (c) Magnified image at interface area, matches with model

Previous low magnification images proved high density at the initial growth region. When exposed under high magnification, stacking faults as well as twins were observed starting from the epitaxial growth. Therefore we deduce that these defects were induced by a combination of lattice mismatch and difference in thermal expansion coefficient, which generated strains at the interface when BP grew.

The high magnification image recorded at a high-density defect region is shown in Fig. 4-9(a)(b). In this region, it is clear to see that stacking faults and dislocations from 3C-SiC did not thread through the epilayer. But compared to the previous image, interfacial stacking was not very smooth and defect such as inclusions and stacking faults divided the epilayer into various domains. The area marked in red rectangular indicated the existence of $B_{12}P_2$, this area was comprised by the stacking of $[11\bar{2}0]$ $B_{12}P_2$ and its twined domains, related by $\frac{1}{6}[1\bar{2}10]$ in distance.

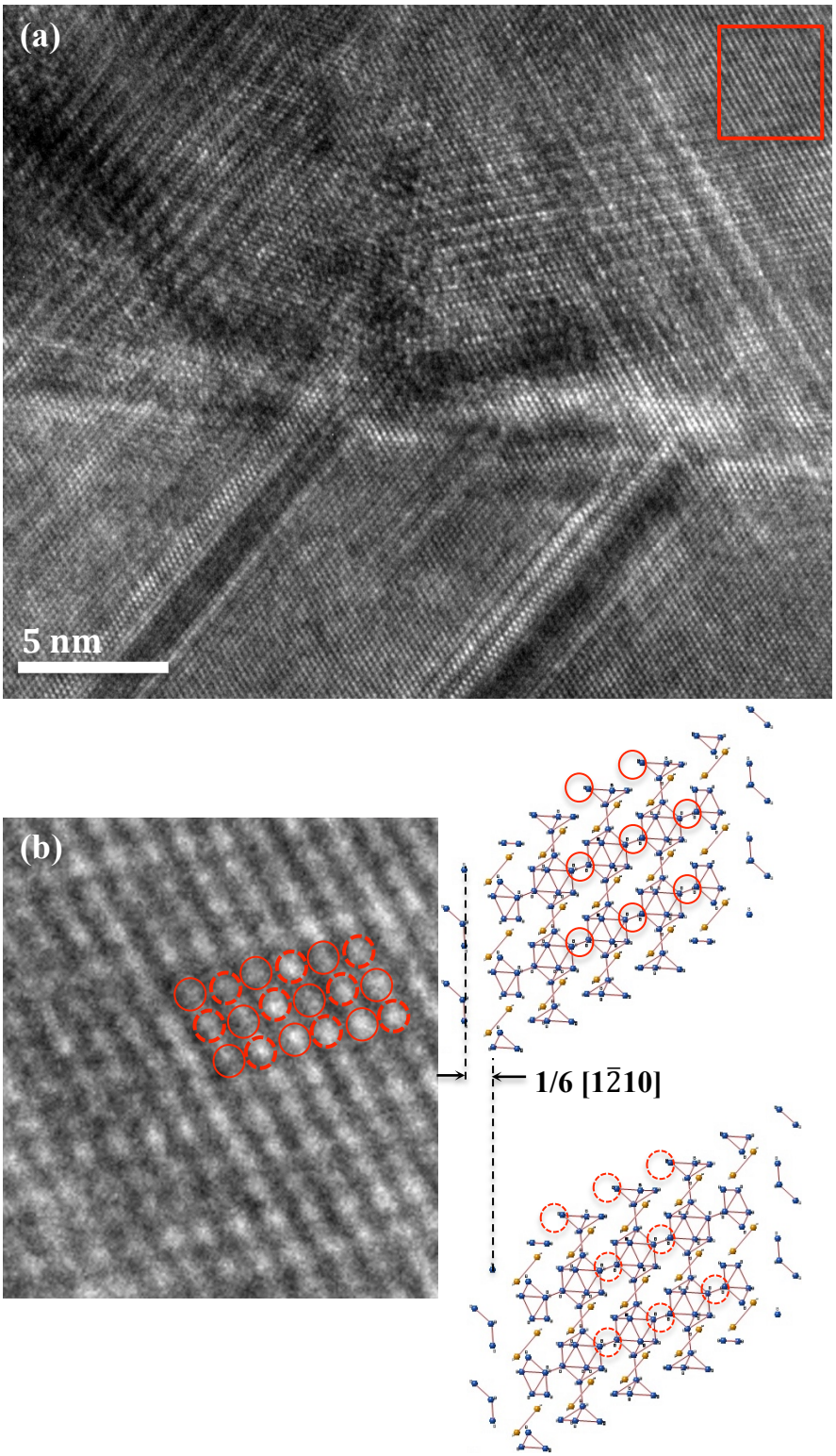

Fig. 4-9 HRTEM images at the interface; (a) HRTEM image recorded at high density defect region. Red rectangular marked the area of $B_{12}P_2$ existence formed by its twins. (b) Magnified image of the defect region matches with ($11\bar{2}0$) projection of $B_{12}P_2$, with its twins formed with a distance of 1/6[$1\bar{2}10$]

4.5 Conclusion

A detailed defect study has been attempted on BP||3C-SiC films. Two growth orientations [100] and [111], temperature, P/B ratio and reaction time are varied parameters for comparison. SWBXT confirmed good single crystalline nature and the epitaxial relationships of each sample. No rotational BP twins were observed. From SEM studies, $(100)_{BP}||(100)_{3C\text{-}SiC}$ achieved much better surface smoothness, and HRXRD further confirmed this observation. Mismatch calculations from rocking curves indicated good relaxation effect of $(100)_{BP}||(100)_{3C\text{-}SiC}$ films. TEM experiments have been conducted for microstructure analysis, from which high density of defects such as dislocations, twins and stacking faults have been observed at initial BP growth region. Smooth atomic connections were realized at the interface since both the epilayer and 3C-SiC buffer possess the same structure and close lattice parameter. High magnification images prove the existence of $B_{12}P_2$ and its twins, which spreads all over the film and has easy transition from (100) BP.

Chapter 5. Defect Studies of CVD Grown BP Epilayers on AlN/Sapphire Substrates

5.1 Outline

A detailed analysis of the crystalline quality and structure in BP epitaxial growth on AlN/sapphire substrates is presented. SWBXT, SEM, HRXRD and TEM experiments have been conducted as a combination. The X-ray topographs revealed single crystalline nature. Diffraction intensity of both (111) BP and (0001) AlN were strong, which indicated good quality of the film. Basic epitaxial relationships were found to be $(0001)<11\bar{2}0>_{AlN}||(111)<1\bar{1}0>_{BP}$ of both on-axis and 1° off-axis towards $[11\bar{2}0]$, rotational BP twins were found and formed by 180° rotation to surface normal. SEM and HRXRD studies indicated desired quality of BP||AlN/sapphire films. Extensive high-precision measurements of relative out-of-plane lattice mismatch have been conducted, and these heterofilms were found to be relaxed with the range from -0.02%~-2.90%. Preliminary results on TEM indicate high quality of the films, with low defect density.

5.2 Introduction

Thick BP films were grown on AlN buffered sapphire substrates using the chemical vapor deposition technique. AlN buffers were grown on sapphire to enhance its stability as well as conduction with BP epitaxy. The difference of coefficient thermal expansion (CTE) and the lattice mismatch between BP and AlN are larger than the BP||SiC system, which indicates that higher density strain-induced defects would occur at the interface region. Consider the buffer condition, both on-axis and 1° off-axis films were deposited, but the difference is not obvious as indicated by the following experimental results.

5.3 Experimental

Boron phosphide films were grown in a horizontal cold walled chemical vapor deposition reactor at an operating pressure of 700 torr. The reactor set-up is similar to that of the previous work on BP film growth on 4H-SiC(0001). Ultra-high purity phosphine (99.9999%) and diborane (1% in H_2) gases were the precursor sources. Hydrogen gas purified through a palladium membrane was used as the carrier gas. BP films were grown on two types of AlN substrates: AlN buffer layers (~2 μm) deposited on on-axis sapphire (0001) substrate and AlN buffer layers (~2 μm) deposited on off-axis sapphire (0001) substrate with 1^o towards $[11\bar{2}0]$ direction. Substrates were heated at 1200 °C under H_2 flow before the BP deposition to clean the surface. After the in-situ H_2 etching, reactant gases were introduced into the carrier gas stream to deposit BP films. The growth temperature varied for 1000, 1100 and 1200 °C and P/B ratio (gas flow rate) were controlled from100 to 200. Films were reacted for 30 minutes. Detailed information of samples are shown in Table. 5-1.

Table. 5-1 Sample information of BP grown on AlN/sapphire substrates

Substrate	Sample #	Temperature (^{o}C)	P/B Ratio	Time	Raman BP peak FWHM (cm^{-1})	XRD BP(111)/ BP(220)
AlN/sapphire,	244	1000			10.8	477
1^{o} off-axis	219	1100	200		7.9	660
along [11$\bar{2}$0]	229	1200		30	6.8	1266
AlN/sapphire,	234	1200	100	min	7.2	6419
on-axis	227		200		7.1	5919

Basic epitaxial relationships, rotational twinning and the general film quality were determined using the SWBXT technique, which was conducted at 3.3.2 Advanced Light Source at Berkeley Lab. The white beam X-ray had wavelength spectrum ranging from 0.6Å to 2.00Å, in which the beam peak had a wavelength of 0.8 Å. The transmission geometry Laue patterns were recorded on STRUCTURIX D3-SC X-ray films at a sample to film distance of 18.5 cm. Simulation of diffraction patterns was processed using the software LauePt. Surface morphology and grain size were analyzed using the SEM at Stony Brook University.

High-resolution X-ray rocking curve measurements were carried on the Bede D1 Diffractometer at Stony Brook University. The Ultima III Diffractometer at Center for Functional Nanomaterials at Brookhaven National Lab was used as assistance for the reciprocal space mapping. Samples were mounted vertically. In case of off-axis polishing along [11$\bar{2}$0] direction, the off-cut direction and magnitude was determined by ω-relative scan of AlN, from which we make sure that the X-ray beam was accurately perpendicular to the (0001) surface of AlN substrate. Followed by the alignment procedure, rocking curves of ω-2θ as well as ω-relative BP were measured.

5.4 Results and discussion

5.4.1 SWBXT and SEM results

Transmission X-ray topography of selected sample is shown in Fig. 5-1. Both the (111) BP and (0006) sapphire shows three-fold structure while AlN diffraction patterns (DPs) show a six-fold structure. Good single crystalline quality was observed in each of the films, with blurred diffraction of BP compared with the AlN DPs. The BP rotational twins were found, with a 180° rotation about [0001]. Epitaxial relationships of both on-axis and 1° off-axis samples are the same: $(0001)\langle 11\bar{2}0\rangle_{AlN} \| (111)\langle 1\bar{1}0\rangle_{BP}$. Due to large strains inside the film, grazing incidence was not effective to observe the microstructure of the films.

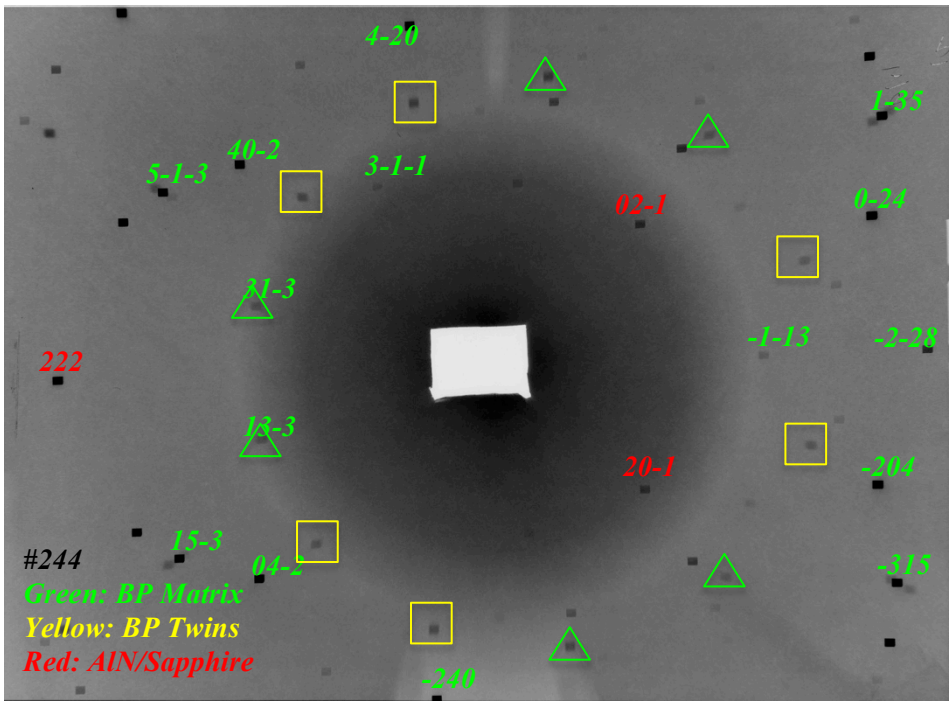

Fig. 5-1 Indexed transmission X-ray topography of BP grown on AlN/sapphire substrate. Green: BP matrix, yellow: BP twins, red: AlN/sapphire

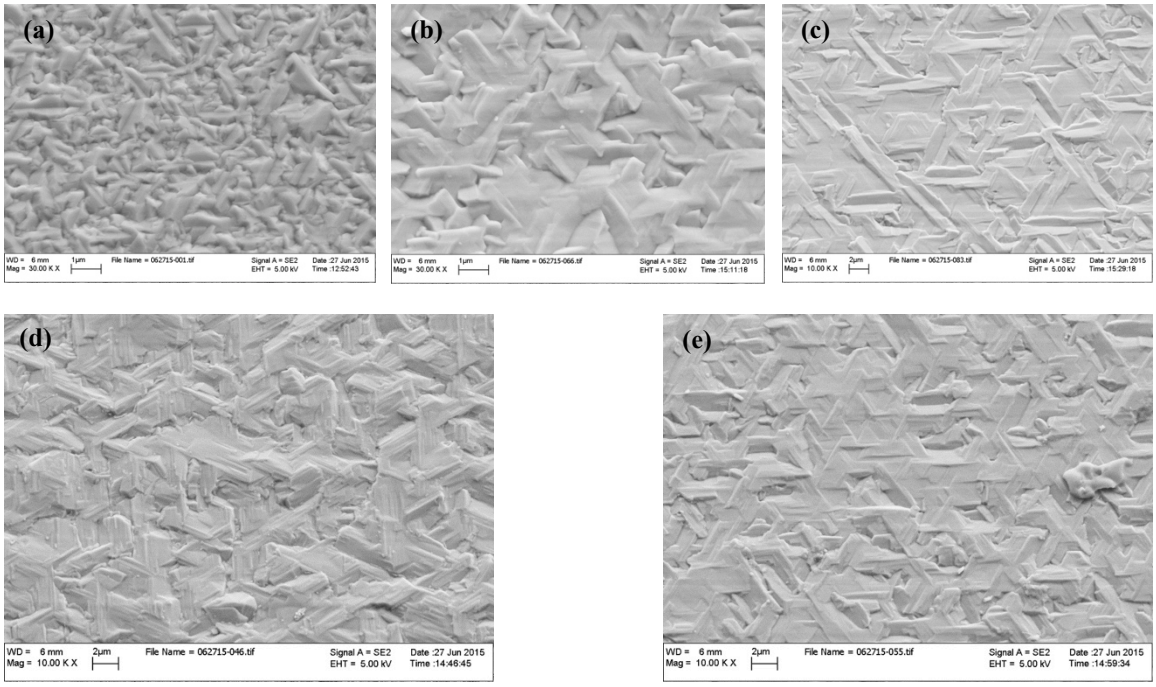

Fig. 5-2 SEM images of BP grown on AlN/sapphire substrates, on-axis AlN: (a)#244, (b)#219, (c)#229, AlN with 1° off-axis along $[11\bar{2}0]$*: (d) #234, (e) #227*

SEM studies helps to analyze the surface morphology of all the samples. Compare the on-axis samples with off-axis ones, surface smoothness were almost the same except a more amorphous structure in sample 244. This indicates that higher temperature is preferred for smoother BP epitaxy. Twinned BP structure was confirmed through SEM images, with triangular feature with a 180° difference.

5.4.2 HRXRD results

High resolution rocking curves of BP||AlN/sapphire samples are shown in Fig. 5-3. Sample 244 has poor quality of BP compared to other samples, with low relative intensity as well as FWHM value. This result corroborates the previous SEM study, that lower temperature is not preferred for high quality BP growth on AlN/sapphire substrates. For other samples, rocking curve width and intensity ratio of BP and AlN indicated similar quality. Since we care more about the BP condition, the AlN/sapphire interface was not investigated. Sample 229 was relatively better with FWHM = 351.5 arcsec. General results confirm that AlN/sapphire substrate is desired for high quality BP deposition.

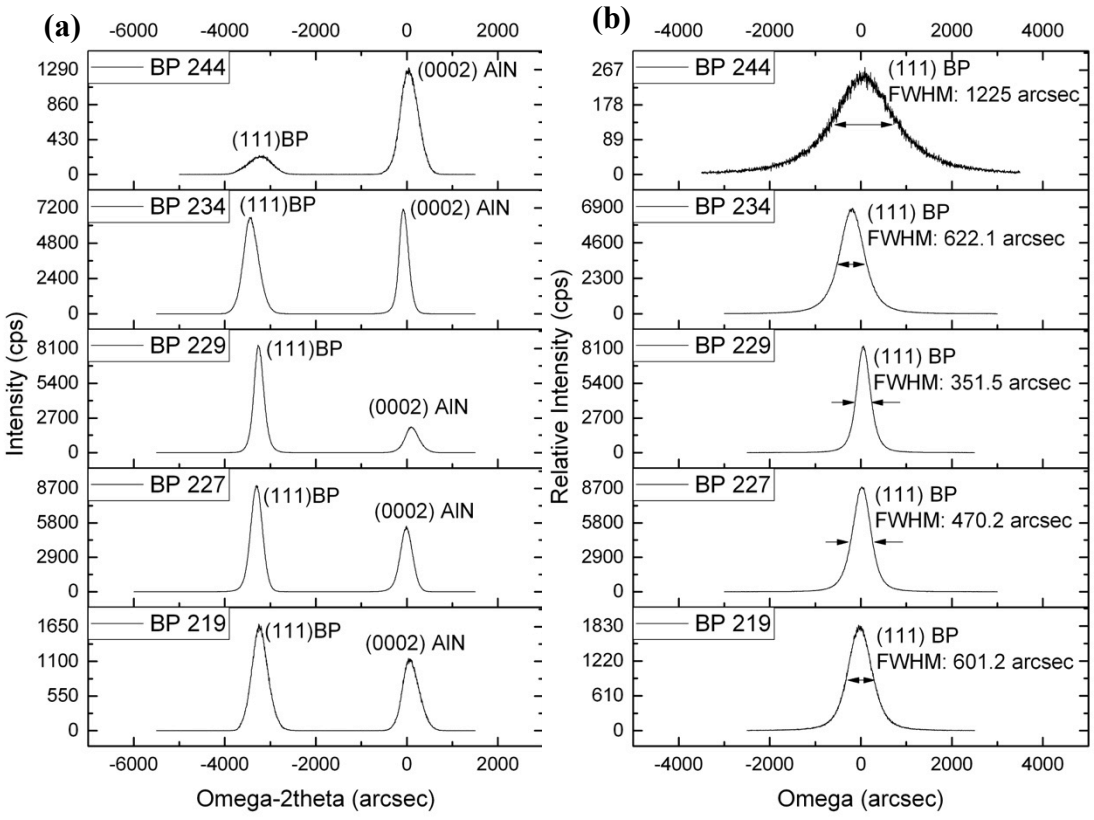

Fig. 5-3 High resolution X-ray rocking curves of BP grown on AlN/sapphire substrates. (a) ω - 2θ scans, left peak (111) BP, right peak (0001) AlN peak, (b) ω - relative scans of (111) BP

Table. 5-2 HRXRD results of BP grown on AlN/sapphire substrates

Substrate	Sample #	Off-cut by HRXRD	FWHM by ω-rel (arcsec)	FWHM by ω-2θ (arcsec)	Theoretical Mismatch	Experimental Mismatch	Out-of-plane Strain
AlN/sapphire 1° off-axis	244	1°	AlN: 532.9 BP: 1255	AlN: 444.9 BP: 550.8	-4.924%	-4.781%	-2.904%
	219	1.3°	AlN: 538 BP: 601.2	AlN: 421.8 BP: 390.3		-4.923%	-0.0203%
	229	1°	AlN: 549.4 BP: 351.5	AlN: 338.7 BP: 248.6		-5.031%	2.173%
AlN/sapphire on-axis	234	-	AlN: 328 BP: 622.1	AlN: 236.4 BP: 380.7		-4.985%	1.239%
	227	-	AlN: 484.5 BP: 470.2	AlN: 305.8 BP: 303		-4.929%	0.102%

Detailed results such as FWHM and lattice mismatch are listed in Table. 5-2. As indicated in previous section, the FWHM from experiment was measured from symmetrical direction. In case of 1° off-axis of AlN buffer layer, the deviation term of rocking curve width is calculated as follows: $\sqrt{\frac{|\gamma_h|}{\gamma_0}} \approx 0.948$. This result indicates that for 1° off-axis of AlN buffer layer, the deviation from symmetrical rocking curve width is only 5.2%, which means our experimental results are close to symmetrical reflection values.

Lattice mismatch was also calculated in c direction (detailed calculation method was shown in 4H-SiC section). Results show that out-of-plane strain in sample 244 is the largest, which indicates that the film was not relaxed well during the growth. Combined with previous analysis, we conclude that higher strains would lead to poorer film quality. For other films, it was observed that sample 219 and 227 were almost relaxed through strain-induced defects, but compare the relative intensity of BP, sample 227 was much better. Combined all the results together, sample 227 and 229 are higher quality ones, which indicates temperature of 1200°C is favored in this material system.

5.5 Conclusion

A combination of techniques have been applied to study the defects in $(111)_{BP}||(0001)_{AlN/sapphire}$ films. SWBXT confirmed good single crystalline nature and epitaxial relationships between BP and AlN. BP rotational twins have been observed in both XRT and SEM images. SEM and HRXRD both confirmed good quality of BP, where the intensity ratio as well as the FWHM of BP/AlN both improved compared with BP||SiC system. High precision lattice mismatch indicates good relaxation effect at the interface. The high quality films are currently being analyzed using TEM at BNL.

Chapter 6. Conclusions and Future Work

6.1 Conclusions

Film quality and the defect structures have been analyzed on four material systems: BP||4H-SiC, BP||6H-SiC, BP||3C-SiC/Si and BP||AlN/sapphire. A combination of characterization techniques has been applied, which includes SWBXT, SEM, HRXRD and TEM. Results help to understand the best growth conditions for high quality BP epitaxy and are listed in Table. 6. All the samples are grown by CVD technique, and growth variables are varied in temperature, reaction time, P/B ratio. Consider the nature of the substrate, 4H-SiC tends to be the best (with avg. FWHM < 300 arcsec). For substrate conditions, 4H-SiC and 6H-SiC with off-cut magnitude are desired for growing high quality BP. The 3C-SiC with (100) growth orientation is preferred. Both on-axis and off-axis AlN buffers have been observed with no obvious difference on quality effect. Consider the growth parameters, we list the parameters for the best quality sample in each group, but this is a general reference since there could be better combinations of growth conditions. Using TEM technique, the microstructure at the interface region has been observed successfully of $(100)_{BP}||(100)_{3C\text{-}SiC}$ sample. It is an effective technique for our samples since they are highly strained. Defects such as $B_{12}P_2$ structure and its rotational twins, dislocations and the stacking faults have been proved to divide the epilayer into multiple domains.

Table. 6-1 Favored parameters for high quality BP growth

Substrate/ Buffer	Nature of Substrates By avg. FWHM (arcsec)	Substrate Condition	Temperature	P/B ratio
4H-SiC	231.316	(0001) with 4° off along [1$\bar{1}$00]	1150°C	10
6H-SiC	922.05	(0001) with 3.5° off along [1$\bar{1}$00]	1150°C	10
3C-SiC	713.16	(100) on-axis	1000°C	100
AlN	486.56	(0001)	1200°C	200

6.2 Future Work

In the future study, it is expected that TEM experiments would be performed on $(100)_{BP}||(100)_{3C\text{-}SiC}$ and $(111)_{BP}||(0001)_{AlN/sapphire}$ samples for detailed analysis, STEM would be applied to determine the defect growth mechanism and the interfacial atomic stacking. Characterization results on $(100)_{BP}||(100)_{3C\text{-}SiC}$ and $(111)_{BP}||(0001)_{AlN/sapphire}$ indicate that these two types of films can be the best for device applications, thus after the TEM analysis is complete, it is expected that testing of thermoelectric properties (resistivity, thermal conductivity, Seebeck coefficient) will be attempted for the real applications in solid state neutron detectors.

References

[1] P. Popper, T. A. Ingles, "Boron Phosphide, a III-V Compound of Zinc-Blende Structure", Nature, No.4569, May 25, 1957, P1075;

[2] Forrest V. Williams and Robert A. Ruehrwein, "The Preparation and Properties of Boron Phosphide and Arsenides", presented in part at the 135th meeting of the American Chemical Society, Boston, Mass., April 7, 1959;

[3] Ting L. Chu, "Boron Arsenide and Boron Phosphide for High Temperature and Luminescent Devices", NASA final technical report, 1969;

[4] R. J. Archer, R. Y. Koyama, E. E. Loebner, and R. C. Lucas, Phys. Rev. Lett. 12, 538;

[5] Shigemi Yugo, Takashi Sato, Tadamasa Kimura, "Thermoelectric figure of merit of boron phosphide", J. Appl. Phys. 46 (9), 842, 1985;

[6] Y. Kumashiro, T. Yokohama, and Y. Ando, "Thermoelectric Properties of Boron and Boron Phosphide CVD Wafers", IEEE, 17th International Conference on Thermoelectrics, 1998;

[7] C. Prasad and M. Sahay, "Electronic Structure and Properties of BP and BAs", Phys. stat. sol. (b) 154, 201 (1989);

[8] E. Schroten, A. Goossens and J. Schoonman, "Photo-and Electroreflectance of Cubic Boron Phosphide", J. Appl. Phys 83, 1660 (1998);

[9] Y. Kumashiro, "Thermophysical Properties of Boron Phosphide Single Crystalline Waafers", The Rigaku Journal, Vol. 7, 1990;

[10] Y. Kumashiro, T. Yokoyama et al. "Electrical and Thermal Properties of $B_{12}P_2$ Wafers", J. Solid State Chemistry 154, 33-38, 2000;

[11] Y. Kumashiro, H. Yoshizawa et al. "Epitaxial Growth of Rhombohedral Boron Phosphide Single Crystalline Films by Chemical Vapor Deposition", J. Solid State Chemistry 133, (1997);

[12] T. L. Chu, J. M. Jackson et al. "Crystals and Epitaxial Layers of Boron Phosphide", J. Appl. Phys 42, 420 (1971);

[13] T. Udagawa, M. Odawara, G. Shimaoka, "High-resolution TEM characterization of MOVPE-grown (111)-BP layer on hexagonal 6H(0001)-SiC", Applied Surface science 244 (2005);

[14] Yu Zhang, Hui Chen et al. "Growth Mechanisms and Defect Structures of $B_{12}As_2$ Epilayers Grown on 4H-SiC Substrates", J. Crystal Growth 352(1), 3-8 (2012);

[15] H. Chen, G. Wang et al. "Defect Structures in $B_{12}As_2$ Epilayers Grown on (0001) 6H-SiC", J. Appl. Phys 103, 123508 (2008);

[16] T. L. Chu, J. M. Jackson and R. K. Smeltzer, "The Crystal Growth of Boron Monophosphide from Metal Phosphide Solutions", J. Electrochem. Soc. Vol 120, 802, 1973;

[17] W. M. Fiest, S. R. Steele, and D. W. Readey "Physics of Thin Films" (G. Hass and-R.E. Thun eds.), 5, 237, Academic Press, New York (1969);

[18] A N Caruso, "The Physics of Solid-state Neutron Detector Materials and Geometries", J. Phys. : Condens. Matter 22 (2010);

[19] T.W. Crane and M. P. Baker, "'Neutron Detectors', in Passive Nondestructive Assay of Nuclear materials," Nuclear Regulatory Commission, NUREG/CR-5550 139, (1991);

[20] P. Rinard, "Neutron Interaction with Matter", in Passive Nondestructive Assay of Nuclear materials, ed. by D. Reilly et al., Nuclear Regulatory Commission, NUREG/CR-5550 357, (1991);

[21] D. S. McGregor et al., "Designs for Thin Film Coated Semiconductor Thermal Neutron Detectors", Nuclear Science Symposium Conference Record, (IEEE 2001), P 2454;

[22] A.N. Caruso, "The Physics of Solid-State Neutron Detector Materials and Geometries ", J. Phys. Condes. Matter **22**, 443201 (2010);

[23] David R. Black and Gabrielle G. Long, "X-ray Topography", practice guide, 2004;

[24] J Guo, Y Yang, F Wu, OY Goue, B Raghothamachar, M Dudley et al., "Direct Determination of Threading Mixed Dislocations in 4H-SiC c-Plane Wafers Grown by PVT Method", ECS Transactions 69 (11), 33-38, 2015;

[25] Y Yang, J Guo, OY Goue, H Wang, F Wu, B Raghothamachar, M Dudley et al., "Double Shockley Stacking Fault Formation in Higher Doping Regions of PVT-Grown 4H-SiC Wafers", ECS Transactions69 (11), 39-46, 2015;

[26] FZ Wu, HH Wang, Y Yang, JQ Guo, B Raghothamachar, M Dudley et al., "Stacking Fault Formation via 2D Nucleation in PVT Grown 4H-SiC", Materials Science Forum 821, 85-89; 2015;

[27] F Wu, H Wang, B Raghothamachar, M Dudley et al., "Characterization of V-shaped Defects in 4H-SiC Homoepitaxial Layers", J. Electronic Materials, 44 (5), 1293-1299, 2015;

[28] H Wang, M Dudley, F Wu, Y Yang, B Ragothamachar et al., "Studies of the Origins of Half-Loop Arrays and Interfacial Dislocations Observed in Homoepitaxial Layers of 4H-SiC", J. Electronic Materials, 44 (5), 1268-1274, 2015;

[29] B Padavala, CD Frye, Z Ding, R Chen, M Dudley, B Raghothamachar et al., "Preparation, Properties and Characterization of Boron Phosphide Films on 4H- and 6H-silicon carbide", Solid State Sciences, 2015;

[30] Beaumont, J.H. and M. Hart, Multiple Bragg Reflection Monochromators for Synchrotron-X Radiation. Journal of Physics E-Scientific Instruments, 1974. 7(10): p. 823-829;

[31] A.R. Lang: Direct observation of individual dislocations by x-ray diffraction, J. Appl. Phys.

29, 597–598 (1958)

[32] C.S. Barrett: A new microscopy and its potentialities, AIME Transactions 161, 15–65 (1945);

[33] W.L. Bond, J. Andrus: Structural imperfections in quartz crystals, Am. Mineral. 37, 622–632 (1952);

[34] G.H. Schwuttke: New x-ray diffraction microscopy technique for study of imperfections in semiconductor crystals, J. Appl. Phys. 36, 2712–2714 (1965);

[34] Balaji Raghothamachar, Michael Dudley, Govindhan Dhanaraj, "X-ray Topography Techniques for Defect Characterization of Crystals", Springer Handbook of Crystal Growth, 42 1425-1450, 2010;

[35] X. R. Huang, "LauePt, A Graphical-user-interface Program for Simulating and Analyzing White-beam X-ray Diffraction Laue Patterns", J. appl. Crystallography, ISSN 0021-8898, 2010.